

# Small-scale lithospheric heterogeneity characterization using Bayesian inference

Itahisa González Álvarez<sup>1</sup> (eeinga@leeds.ac.uk, @seismowaves)

Sebastian Rost<sup>1</sup> (s.rost@leeds.ac.uk)

Andy Nowacki<sup>1</sup> (a.nowacki@leeds.ac.uk)

Neil D. Selby<sup>2</sup> (neil@blacknest.gov.uk)

<sup>1</sup>School of Earth and Environment, University of Leeds, Leeds, LS2 9JT, UK.

<sup>2</sup>Blacknest, AWE, Reading, RG7 4RS, UK

This manuscript has been submitted for publication in **Geophysical Journal International** and is undergoing peer-review. Please note that the manuscript has not been formally accepted for publication. Subsequent versions of this manuscript may have slightly different content. If accepted, the final version of this manuscript will be available via the Peer-review Publication DOI link on this webpage. Please feel free to contact the authors; We welcome feedback.

# Small-scale lithospheric heterogeneity characterization using Bayesian inference.

Itahisa González Álvarez<sup>1</sup>, Sebastian Rost<sup>1</sup>, Andy Nowacki<sup>1</sup>,  
and Neil D. Selby<sup>2</sup>

<sup>1</sup>School of Earth and Environment, University of Leeds, LS2 9JT, UK. E-mail: eeinga@leeds.ac.uk

<sup>2</sup>Blacknest, AWE, Reading, RG7 4RS, UK

## SUMMARY

Observations from different disciplines have shown that our planet is highly heterogeneous at multiple scale lengths. Still, many seismological Earth models tend not to include any small-scale heterogeneity or lateral velocity variations, which can affect measurements and predictions based on these homogeneous models. In this study, we describe the lithospheric small-scale heterogeneity structure in terms of the intrinsic, diffusion and scattering quality factors, as well as an autocorrelation function, associated with a characteristic scale length ( $a$ ) and root mean square (RMS) fractional velocity fluctuations ( $\epsilon$ ). To obtain this characterization, we combined a single-layer and a multi-layer energy flux models with a new Bayesian inference algorithm. Our synthetic tests show that this technique can successfully retrieve the input parameter values for 1- or 2-layer models and that our Bayesian algorithm can resolve whether the data can be fitted by a single set of parameters or a range of models is required instead, even for very complex posterior probability distributions. We applied this technique to three seismic arrays in Australia: Alice Springs array (ASAR), Warramunga Array (WRA) and Pilbara Seismic Array (PSA). Our single-layer model results suggest intrinsic and diffusion attenuation are strongest for ASAR, while scattering and total attenuation are similarly strong for ASAR and WRA. All quality factors take higher values for PSA than for the other two arrays, implying that the structure beneath this array is less attenuating and heterogeneous than for ASAR or WRA. The multi-layer model results shows the crust is more heterogeneous than the lithospheric mantle for all

arrays. Crustal correlation lengths and RMS velocity fluctuations for these arrays range from  $\sim 0.2 - 1.5$  km and  $\sim 2.3 - 3.9$  % respectively. Parameter values for the upper mantle are not unique. Both low ( $< 2$  km) and high ( $> 5$  km) correlation length values are equally likely and  $\epsilon$  takes values up to  $\sim 6\%$  and  $\sim 7\%$  for ASAR and WRA respectively and up to  $\sim 3\%$  for PSA. We attribute the similarities in the attenuation and heterogeneity structure beneath ASAR and WRA to their location on the proterozoic North Australian Craton, as opposed to PSA, which lies on the archaean West Australian Craton. Differences in the small-scale structure beneath ASAR and WRA can be ascribed to the different tectonic histories of these two regions of the same craton. Overall, our results highlight the suitability of this technique for future scattering and small-scale heterogeneity studies, since our approach allows us to obtain and compare the different quality factors, while also giving us detailed information about the trade-offs and uncertainties in the determination of the scattering parameters.

**Keywords:** Structure of the Earth, Australia, statistical methods, coda waves, seismic attenuation, wave scattering and diffraction.

# 1 INTRODUCTION

2 The Earth is heterogeneous on a variety of scales, ranging from the grain scale  
3 to scales of hundreds of kilometers. This heterogeneity is evident in data from  
4 geo-disciplines with varying sensitivity to scales, such as geochemistry, mineralogy  
5 or seismology (e.g. Wu and Aki, 1988). Due to the seismic wavelengths, most  
6 seismological Earth models are laterally homogeneous or smoothly varying, with a  
7 lack of small-scale heterogeneity (e.g. Helmberger, 1968; Dziewonski and Anderson,  
8 1981; Kennett and Engdahl, 1991; Randall, 1994). This limits our understanding  
9 of high-frequency seismic wave propagation and challenges in seismic imaging of  
10 small-scale heterogeneities remain.

11 Many seismic studies published before the 1970s were based on laterally ho-  
12 mogeneous Earth models (e.g. Alexander and Phinney, 1966) which were able to  
13 explain the propagation of long period signals, but failed to explain high frequency  
14 seismograms. Aki (1969) showed that the power spectra of coda waves for a given  
15 station are independent of epicentral distance and earthquake magnitude. He  
16 proposed that codas were caused by backscattered energy from discrete hetero-  
17 geneities randomly distributed beneath the stations. The presence and shape of  
18 the coda strongly depends on the heterogeneity structure and the geology beneath  
19 the station. Later studies (e.g. Aki and Chouet, 1975; Rautian and Khalturin,  
20 1978) showed that the stable decay in coda wave amplitude was also indepen-  
21 dent of epicentral distance and source mechanism, fully supporting the scattering  
22 hypothesis.

23 Methods to study heterogeneity and scattering within the Earth vary depend-  
24 ing on the type of the heterogeneity. Many seismological studies use deterministic  
25 methods to characterize the structure of the Earth (e.g. Christensen and Mooney,  
26 1995; Zelt and Barton, 1998) or to find individual scatterers and try to obtain their

27 particular characteristics and locations (e.g. Etgen et al., 2009). Marchenko imag-  
28 ing (e.g. Thorbecke et al., 2017; van der Neut et al., 2015) or migration techniques  
29 (e.g. Etgen et al., 2009) are often used in reflection seismology to study shallow  
30 structure and are a good example of deterministic methods. These techniques tend  
31 to have limited spatial resolution due to the wavelength of the studied waves and  
32 do not take into account small-scale heterogeneities (on the order of magnitude of  
33 the wavelength), therefore failing to explain or reproduce the complex coda waves  
34 we see in seismograms. Therefore, a stochastic description of the heterogeneity dis-  
35 tribution is often necessary for scattering studies (e.g. Korn, 1990, 1997; Margerin,  
36 2005; Hock et al., 2004; Ritter et al., 1998).

37 A stochastic approach (e.g. Frankel and Wennerberg, 1987; Shapiro and Kneib,  
38 1993; Hock et al., 2004) gives a statistical description of the structure and deter-  
39 mines the integrated effect of heterogeneity on seismic waves propagating through  
40 it, so the characteristics and locations of individual scatterers are not relevant.  
41 Studies (e.g. Aki, 1973; Flatté and Wu, 1988; Langston, 1989) showed the crust  
42 and lithospheric heterogeneity to be statistically complex and the necessity of  
43 heterogeneous Earth models that were capable of explaining not only the main  
44 waveforms but also coda waves. Seismic wave propagation through heterogeneous  
45 stochastic media can be described using several methods. Single-scattering pertur-  
46 bation theory (e.g. Aki and Chouet, 1975; Sato, 1977, 1984) considers scattering to  
47 be a weak process and coda waves the superposition of single scattered waves gen-  
48 erated at randomly distributed heterogeneities within the Earth. It often makes  
49 use of the Born approximation (e.g. Sato et al., 2012), a first-order perturbation  
50 condition which does not take into account the energy loss from the primary waves.  
51 As a result, energy is not conserved in the scattering process (e.g. Aki and Chouet,  
52 1975). Radiative transfer theory, initially developed for light propagation (Chan-

53 drasekhar, 1950) and later modified for and applied to seismology, has been used  
54 in several scattering and attenuation studies (e.g. Margerin, 2005; Sato et al., 2012;  
55 Wu, 1985; Fehler et al., 1992).

56 In this study, we combine two stochastic methods, the single layer modified  
57 Energy Flux Model (EFM, Korn, 1990) and the depth dependent Energy Flux  
58 Model (EFMD, Korn, 1997), with a Bayesian inversion algorithm which allows us  
59 to characterise small-scale lithospheric heterogeneity by fully exploring the scatter-  
60 ing parameter space and obtain information about the trade offs and uncertainties  
61 in the determination of the parameters. We applied these methods to a large  
62 dataset of teleseismic events recorded at three seismic arrays of the Australian  
63 National Seismic Network: Alice Springs Array (ASAR) and Warramunga Ar-  
64 ray (WRA), which are primary seismic arrays from the International Monitoring  
65 System network, and Pilbara Seismic Array (PSA).

## 66 2 METHODS

67 We use the random medium approach, which considers the propagation of seismic  
 68 waves through a background medium with constant velocity and random het-  
 69 erogeneities distributed according to a given autocorrelation function (ACF). This  
 70 ACF depends on the RMS fractional velocity fluctuations,  $\epsilon$ , and the characteristic  
 71 or correlation length,  $a$ , which defines the spatial variation of the heterogeneities.  
 72 By obtaining these parameters, it is possible to obtain a statistical description  
 73 of the sampled structure that reveals the strength of the scattering experienced  
 74 by seismic waves. The modified Energy Flux Model (EFM) and depth-dependent  
 75 Energy Flux Model (EFMD) can be used for both weak and strong scattering (e.g.  
 76 Korn, 1990; Hock and Korn, 2000; Hock et al., 2004) and allow determining the  
 77 best-fitting ACF of the heterogeneous medium. Both methods work under the as-  
 78 sumption of planar wavefronts and vertical or near-vertical incidence from below  
 79 on a single scattering layer (EFM) or stack of layers (EFMD), conditions well met  
 80 by teleseismic events.

81 Here we present a short introduction to the EFM and EFMD. Full details  
 82 about the methods can be found in Korn (1990), Korn (1997), Hock and Korn  
 83 (2000) and Hock et al. (2004).

### 84 2.1 The Modified Energy Flux Model for a single scat- 85 tering layer

86 When a plane wavefront enters a heterogeneous unlayered medium from below,  
 87 part of the energy propagates with the ballistic wavefront, while part forms the  
 88 forward scattered coda energy that arrives later at the surface and some energy  
 89 scatters back into the half-space. Total energy  $E_{tot}$  is conserved in this process

90 and we can write it in terms of frequency,  $\omega$ , and time,  $t$ , as

$$E_{tot}(\omega, t) = E_d(\omega, t) + E_c(\omega, t) + E_{diff}(\omega, t), \quad (1)$$

91 with  $E_d$  being the energy of the direct wave,  $E_c$  the energy transferred from  
 92 the direct wave into the coda (forward scattered) and  $E_{diff}$  the energy diffusion  
 93 (backscattering) from the current layer back into the half-space. The energy that is  
 94 transferred from the incoming wavefront to the scattered coda and the backscat-  
 95 tering to the half-space can be expressed as an energy loss for the direct wave,  
 96 controlled by a quality factor  $Q_s$  for scattering and  $Q_{diff}$  for diffusion. To take  
 97 into account anelastic (intrinsic) attenuation, we use the quality factor  $Q_i$ . The  
 98 EFM assumes spatially homogeneous coda energy within the scattering layer. En-  
 99 ergy transfer into the coda due to scattering or anelastic losses stops once the  
 100 ballistic wave leaves the scattering layer after totally reflecting at the free surface,  
 101 while diffusion out of the scattering layer can continue after that.

102 A linear least-squares fit of the theoretical coda power spectral density allows  
 103 us to calculate the coda decay rate,  $a_1$ , and its amplitude at zero time,  $a_0$  (Korn,  
 104 1990, 1993). The values of  $Q_i$  and  $Q_{diff}$  at 1 Hz,  $Q_{i0}$  and  $Q_{d0}$ , can be obtained  
 105 from values of  $a_1$  at different frequencies via

$$a_1(\omega) = -2\pi[Q_{d0}^{-1} + Q_{i0}^{-1}(\omega/2\pi)^{1-\alpha}] \log_{10} e, \quad (2)$$

106 where  $\alpha$  is the exponent controlling the frequency dependence of  $Q_i$  (Korn, 1990,  
 107 Eq. 17). Eqs. 16 and 17 from Korn (1990) allow us to determine  $Q_{diff}$  and  $Q_i$   
 108 at different frequency bands. Laboratory measurements of  $\alpha$  have shown that it  
 109 probably remains below 1 for most of the frequency range considered here (Korn,  
 110 1990, and references therein). Our attempts at obtaining  $\alpha$  as a third free param-

111 eter in the least-squares inversion of Eq. 2 revealed a very complicated trade-off  
 112 with  $Q_{i0}$  and  $Q_{d0}$ , with high values of  $\alpha$  corresponding to negative values of  $Q_{i0}$   
 113 and/or  $Q_{d0}$ . Therefore, we limited  $\alpha$  to the range of 0.0 - 0.6, in steps of 0.1, and  
 114 chose the value that minimised the misfit to the data. Both our results and those  
 115 of Korn (1990) show that  $\alpha$  has a strong effect on  $Q_i$  but only weakly affects  $Q_{diff}$ .  
 116 The impossibility to fully invert for  $\alpha$  makes it difficult to accurately calculate  $Q_i$   
 117 with the EFM. However, given that  $Q_i$  is generally much larger than  $Q_{diff}$ , since  
 118 diffusion becomes more important with increasing source distance (Korn, 1990),  
 119 we can expect the effect of anelasticity on coda levels to be small.

120 The coda amplitude at zero time,  $a_0$ , is related to  $Q_s$  through

$$Q_s \approx 2I_D\omega 10^{-a_0}, \quad (3)$$

121  $I_D$  being the integral of the squared amplitude envelope,  $A^2(t;\omega)$ , over the time  
 122 window of the direct wave arrival (Hock and Korn, 2000). We can then use the  
 123 relationships between  $Q_s^{-1}$  and the structural parameters for different types of  
 124 ACFs obtained by Fang and Müller (1996) to determine the type of ACF that fits  
 125 the data best, as well as a first estimation of the correlation length ( $a$ ) and the  
 126 RMS velocity fluctuations ( $\epsilon$ ) for a single scattering layer.

127 Finally, the total quality factor,  $Q_{tot}$ , can be calculated as:

$$\frac{1}{Q_{tot}} = \frac{1}{Q_{diff}} + \frac{1}{Q_i} + \frac{1}{Q_s} \quad (4)$$

128 The eight different one octave-wide frequency bands we used in our analysis  
 129 for both methods are shown in Table 1.

**Table 1:** List of all frequency bands used in this study.

Frequency band	A	B	C	D	E	F	G	H
Minimum frequency (Hz)	0.5	0.75	1	1.5	2	2.5	3	3.5
Maximum frequency (Hz)	1.0	1.5	2	3	4	5	6	7

## 130 2.2 The Energy Flux Model for depth-dependent het- 131 erogeneity

132 Korn (1997) modified the EFM to include depth-dependent heterogeneity. In this  
133 model, a plane wavefront enters a stack of  $N$  heterogeneous layers from below.  
134 Each layer  $j$  has its own characteristic transit time  $\delta t_j$  and scattering quality  
135 factor  $Q_{s_j}$ , which is calculated from the structural parameters  $a_j$  and  $\epsilon_j$  (Fig. 1)  
136 using the analytical approximation for isotropic exponential media obtained by  
137 Fang and Müller (1996). The stack of layers is symmetric with respect to the  
138 free surface, which is located at the center of the stack to take into account the  
139 reflection of the wavefront.

140 For a given angular frequency  $\omega_c$ , the normalised coda energy envelope of a  
141 velocity seismogram at the free surface is computed from the squared amplitude  
142 envelope  $A^2(t; \omega_c)$  and is related to the energy balance within the different layers  
143 in the model through

$$\sqrt{\frac{A^2(t; \omega_c)}{I_D}} = \sqrt{\frac{2E_{C_N}(t; \omega_c)}{t_N E_D(t_N; \omega_c)}}, \quad (5)$$

144 with  $E_{C_N}(t; \omega_c)$  being the spectral coda energy density of the layer containing the  
145 free surface,  $t_N$  the traveltime from the bottom of the stack of layers to the free  
146 surface and  $E_D(t; \omega_c)$  the energy density of the direct wave at the free surface.  $Q_s$   
147 and  $Q_i$  control the decay of the direct wave energy over time due to scattering and

148 intrinsic attenuation via

$$E_D(t_j; \omega) = E_D(t_{j-1}; \omega_c) e^{-\omega(t_j - t_{j-1})(Q_{s_j}^{-1} + Q_{i_j}^{-1})}, \quad (6)$$

149 where  $t_j$  represents the one-way travel time through each layer. The energy balance  
 150 within layer  $j$  ( $j = 1, \dots, N$ ) is represented by

$$\begin{aligned} \frac{dE_{C_j}}{dt} = & -\frac{1}{4\delta t_j} E_{C_j}(t) H(t - t_j) \\ & -\frac{1}{4\delta t_j} E_{C_j}(t) H(t - t_{j-1}) \\ & +\frac{1}{4\delta t_{j-1}} E_{C_{j-1}}(t) H(t - t_{j-1}) \\ & +\frac{1}{4\delta t_{j+1}} E_{C_{j+1}}(t) H(t - t_j) \\ & -\frac{\omega}{Q_{i_j}} E_{C_j}(t) H(t - t_{j-1}) \\ & +\frac{\omega}{Q_{s_j}} E_D(t) H(t - t_{j-1}) H(t_j - t) \end{aligned}, \quad (7)$$

151 where  $H$  is the Heaviside function. The first two terms of Eq. 7 describe the energy  
 152 flux from layer  $j$  to the layers above and below, while the next two terms describe  
 153 the opposite flux from the neighbouring layers into layer  $j$ . The last two terms  
 154 represent the anelastic or intrinsic energy loss and the direct wave energy input  
 155 into the layer. In practice, for a given model  $\mathbf{m}$ , comprising a single value of  $a$  and  
 156  $\epsilon$  for each layer in the stack,  $E_D$  is calculated for each time sample using Eq. 6,  
 157 starting from the measured energy value at the free surface. Then, the system of  
 158 linear differential equations in Eq. 7 is solved for each layer in the model. Finally,  
 159 synthetic coda envelopes are calculated for each frequency band using Eq. 5.

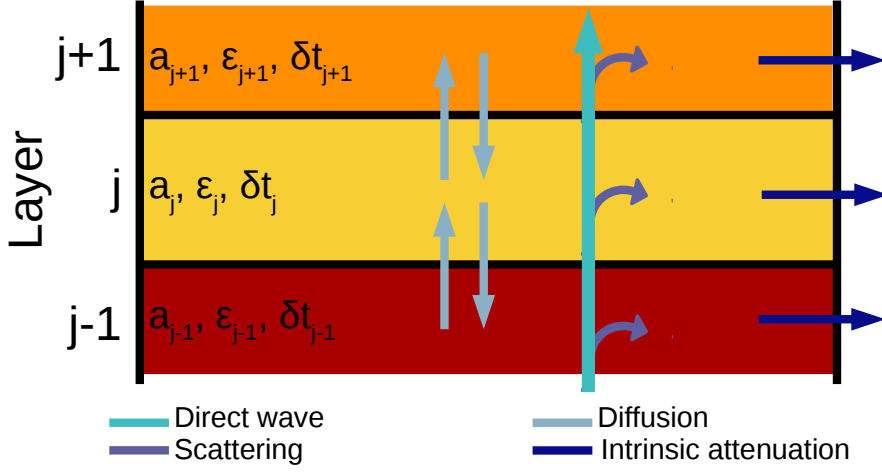


Figure 1: Total energy balance for layer  $j$ , according to the EFMD. (After Korn, 1997).

### 160 2.2.1 Bayesian inference

161 We use a Bayesian approach to obtain the values of the structural parameters for  
 162 each layer in the model (e.g. Tarantola, 2005). In this approach, the aim is not to  
 163 obtain a best fitting model, but to test a large number of models with parameters  
 164 drawn from a prior probability distribution  $p(\mathbf{m})$  (or prior) defined by our previous  
 165 knowledge on them. In our case, we assume we have no previous knowledge on  
 166 the value of the parameters and use a uniform prior.

167 The likelihood associated with model  $\mathbf{m}$ ,  $p(\mathbf{d}|\mathbf{m})$ , is the probability of observing  
 168 our data,  $\mathbf{d}$ , given the model parameters in  $\mathbf{m}$ . We used the Mahalanobis distance  
 169  $\Phi(\mathbf{m})$  (Mahalanobis, 1936) between  $\mathbf{d}$ , with variance-covariance matrix  $\mathbf{C}$ , and the  
 170 synthetic envelopes  $g(\mathbf{m})$ , to calculate the fit to our data:

$$\Phi(\mathbf{m}) = (g(\mathbf{m}) - \mathbf{d})^T \mathbf{C}^{-1} (g(\mathbf{m}) - \mathbf{d}), \quad (8)$$

171 which we then applied to the calculation of the likelihood of model  $\mathbf{m}$ :

$$p(\mathbf{d}|\mathbf{m}) = \frac{1}{\sqrt{(2\pi)^n |\mathbf{C}|}} \exp\left(\frac{-\Phi(\mathbf{m})}{2}\right) \quad (9)$$

172 Bayes' theorem (Bayes, 1763) allows us to calculate the corresponding sample of  
 173 the posterior probability distribution (or posterior), that is, the probability density  
 174 associated with model  $\mathbf{m}$ , or  $p(\mathbf{m}|\mathbf{d})$ :

$$p(\mathbf{m}|\mathbf{d}) \propto p(\mathbf{d}|\mathbf{m})p(\mathbf{m}) \quad (10)$$

175 We create an initial model by selecting a random value for the correlation length  
 176 and velocity fluctuations in all layers in the  $(a_{min}, a_{max})$  or  $(\epsilon_{min}, \epsilon_{max})$  intervals,  
 177 with  $a_{min} = 0.2\lambda_{min}$  [m],  $a_{max} = 2\lambda_{max}$  [m] ( $\lambda_{min}$  and  $\lambda_{max}$  being the mini-  
 178 mum and maximum wavelengths in the layer, depending on signal frequency and  
 179 background velocity),  $\epsilon_{min} = 4.5 \cdot 10^{-3}$  % and  $\epsilon_{max} = 10$  %. These maximum  
 180 and minimum values were chosen considering the relevant range for detectable  
 181 scattering while being geologically feasible (e.g Korn, 1993; Hock et al., 2004).

182 We then applied the Metropolis-Hastings algorithm (Metropolis and Ulam,  
 183 1949; Metropolis et al., 1953; Hastings, 1970) to sample the posterior probability  
 184 distribution and generate our ensemble of solution models. This way, at every  
 185 time step, this Markov Chain Monte Carlo (MCMC) algorithm generates a new  
 186 model  $\mathbf{m}'$  by randomly choosing one of the parameters in the previous model ( $\mathbf{m}$ )  
 187 and updating its value by adding a random number in the  $(-\delta a, \delta a)$  or  $(-\delta \epsilon, \delta \epsilon)$   
 188 interval, with  $\delta a$  and  $\delta \epsilon$  being the step size for correlation length and RMS velocity  
 189 fluctuations respectively. In case the new value of the parameter exceeds the  
 190 boundaries defined by  $(a_{min}, a_{max})$  or  $(\epsilon_{min}, \epsilon_{max})$ , the distance  $\Delta$  to the boundary  
 191 is calculated and the new parameter value is forced to bounce back into the valid

192 parameter range by the same distance  $\Delta$ . The algorithm then takes model  $\mathbf{m}'$  and  
 193 uses Eqs. 7 and 5 to obtain the corresponding synthetic envelopes. In order to  
 194 decide whether to accept or reject the new model, the algorithm uses the posterior  
 195 probability exponent (Eq. 9),  $\Phi(\mathbf{m})/2$ , called here the *loglikelihood*,  $L$ , associated  
 196 with model  $\mathbf{m}$ , as an estimator of the likelihood and the goodness of the fit to  
 197 the data. Thus, if  $L(\mathbf{m})/L(\mathbf{m}') \geq 1$ ,  $\mathbf{m}'$  will be accepted. If  $L(\mathbf{m})/L(\mathbf{m}') < 1$ ,  
 198 however, it will only be accepted if  $\exp(L(\mathbf{m}) - L(\mathbf{m}')) \geq q$ ,  $q$  being a random  
 199 number between 0 and 1. This algorithm ensures that parameter values closer  
 200 to the true value have high likelihoods and are accepted more often than values  
 201 further from the true value. The acceptance rate (AR) represents the percentage  
 202 of times new parameter values were accepted through the Markov chain. There  
 203 are several criteria defining what the value of the AR should be, most of them  
 204 making assumptions about the properties of the target distributions (e.g. Brooks  
 205 et al., 2011). In our case, since we do not have any a priori information about  
 206 the posterior distributions, we aimed at AR values between 30–60 %. Finally we  
 207 calculate the 5- to 95- percentile range (PR) for each parameter in each layer in  
 208 the model from our ensemble of accepted models.

209 For more detailed descriptions of Bayesian inference and MCMCs, we refer the  
 210 reader to Tarantola (2005) or Brooks et al. (2011).

### 211 **2.2.2 Synthetic tests**

212 We tested our EFMD inversion code with five different synthetic datasets, with  
 213 varying number of layers and parameter values. These models, together with a  
 214 summary of our synthetic tests results, are shown in Table 2. In all of them,  
 215 we used Pilbara Seismic Array (PSA, Section 3) as a test array and obtained its  
 216 velocity model and Moho and lithospheric depths from the Australian Seismological

217 Reference Model (AuSREM, Kennett and Salmon, 2012; Kennett et al., 2013;  
 218 Salmon et al., 2013b), although our results should be applicable to all arrays.  
 219 Frequency bands used are listed in Table 1.

220 Figures 2, 3 and 4 below, and S1 and S2 in the Supplementary Material,  
 221 illustrate the results from our synthetic tests for Models 1 to 5 (Table 2). In  
 222 order to test the convergence of our algorithm, we ran three independent Markov  
 223 chains for each model, with a total of 3 million iterations (parameter combinations  
 224 tested) for the single layer model, 9 million for the 2-layer models, and 15 million  
 225 for the 3-layer model. In all of them, for each chain, we discarded the models  
 226 corresponding to the burn-in phase, during which the algorithm is not efficiently  
 227 sampling the posterior probability distribution and models are still affected by the  
 228 random initialization of the Markov chain. In order to define the point at which the  
 229 algorithm reached convergence and the burn-in phase ended, we first calculated the  
 230 mean loglikelihood value in the second half of the chain (during which the algorithm  
 231 is stable) and then subtracted 5% off that value. We consider the algorithm has  
 232 converged the first time it accepts a model with loglikelihood  $L$  equal or higher  
 233 than this value. Our threshold was defined based on the observation, in test runs of  
 234 the EFMD, that  $L$  generally remained stable after reaching the defined threshold  
 235 for the first time.  $L$  provides an estimation of the goodness-of-fit of the synthetic  
 236 data to our real data and takes negative values, meaning fits improve as  $L$  gets  
 237 closer to zero (Eq. 9). In terms of parameter values, we consider that a narrow  
 238 5–95 percentile range (PR) points to clearly determined values of the structural  
 239 parameters, while wide 5–95 PRs would suggest multiple parameter values are  
 240 equally likely and good at fitting our data.

241 For Model 1, with a single layer encompassing the entire lithosphere, all three  
 242 chains reached stability and converged within 10000 iterations. Panels d–f in Fig.

**Table 2:** Summary of the synthetic model layering and our synthetic tests results. For each model, we include the 5–95 percentile range (PR) and the acceptance rate (AR) for each parameter, as well as the maximum loglikelihood ( $L$ ) found during the inversion.

Model	Number of layers	Layer number	Input model		Correlation length ( $a$ )		RMS velocity fluctuations ( $\epsilon$ )		Maximum $L$
			$a$ (km)	$\epsilon$ (%)	5 – 95 PR (km)	AR (%)	5 – 95 PR (%)	AR (%)	
1	1	1	5.0	5.0	4.99 – 5.05	23	4.99 – 5.00	8	-2.5
2	2	1	2.0	5.0	1.7 – 2.4	12	4.8 – 5.3	47	-0.02
		2	3.0	4.0	2.8 – 3.4		3.9 – 4.1		
3	2	1	1.0	7.0	1.00 – 1.01	51	6.95 – 7.02	47	-0.03
		2	6.0	1.0	7 – 32		1.0 – 1.8		
4	2	1	6.0	1.0	6 – 25	50	1.0 – 1.8	51	-1.3
		2	1.0	7.0	0.998 – 1.002		6.998 – 7.003		
5	3	1	1.0	4.0	1 – 23	52	0.1 – 4.7	31	-0.02
		2	2.0	3.0	1 – 21		0.6 – 6.1		
		3	4.0	2.0	3 – 30		1.8 – 3.3		

243 2 show our posterior probability density functions (PDFs) for each parameter, as  
244 well as the joint PDF. In both cases, the distributions are approximately Gaus-  
245 sian and symmetric, with the 5–95 PR being  $\sim 0.06$  km and  $\sim 0.01\%$  wide for  
246 the correlation length and RMS velocity fluctuations respectively (Table 2), which  
247 indicated that the range of suitable values of the parameters is very well defined.  
248 The algorithm slightly overestimates the correlation length and underestimates the  
249 RMS velocity fluctuations, with the input value of the parameter being included  
250 in the 5–95 PR for the latter but not for the former (Table 2, Fig. 2). However,  
251 the difference between the central value of the PDFs and the true value of the  
252 parameter is  $< 0.4\%$  for both the correlation length and the RMS velocity fluc-  
253 tuations. Graphs on the right hand side of Fig. 2 (panels g–n) show histograms  
254 of the synthetic envelopes for our ensemble of accepted models for all frequency  
255 bands. As frequency increases, both envelope amplitudes and width of the ensem-  
256 ble of synthetic envelopes increase too. However, in all cases, the highest density  
257 of envelopes, indicated by a dark brown color, is found in a very narrow line that  
258 matches the input data envelopes, not only in the time window used for the fit  
259 (shadowed area in the plots), but also outside of it.

260 Model 2 contains two layers, representing the crust and lithospheric mantle.

261 Our three chains converged in less than 120000 iterations and remained stable for  
 262 the rest of the inversion, as shown in panels a–c in Fig. 3. Panels d–i in this figure  
 263 summarise our results. In this case, the PDFs for the parameters in both layers  
 264 are narrow (the 5–95 PR is  $< 0.7$  km wide at most for  $a$  and  $< 0.5\%$  for  $\epsilon$ ) and  
 265 approximately centered around the input values, even if they are not Gaussian and  
 266 show some local maxima. The true values of the parameters lie within the 5–95  
 267 PR in all cases, near the center of the joint PDFs, and the maximum difference  
 268 between the input values and the absolute maxima of the PDFs is 2%. Panels j–q  
 269 in Fig. 3 indicate fits to the synthetic data are good, since they show again that  
 270 the largest concentration of synthetic envelopes for all frequencies coincides with  
 271 the input data envelopes.

272 Models 3 and 4 have the same interface structure as model 2 (Table 2) and  
 273 investigate high contrast situations in which a strong heterogeneity layer is above  
 274 or below a layer containing weak heterogeneities respectively. Figs. S1 and S2  
 275 summarise our results and can be found in the Supplementary Material. In both  
 276 cases, the chains reached stability within 11000 iterations. Posterior PDFs for the  
 277 strongly scattering layer are approximately Gaussian and narrow for both models  
 278 3 and 4, with maxima that deviate from the input parameter values by 0.4%  
 279 at most (Table 2). The weakly scattering layer, however, is poorly resolved for  
 280 both models. The posterior PDFs for this layer are very similar in both cases  
 281 and clearly non-Gaussian. They show multiple maxima that do not correspond  
 282 to the input parameter values, which widens the 5–95 PR, especially for  $a$ . The  
 283 RMS velocity fluctuation values seem to be constrained to the range from 0.5–  
 284 1.9 % for both models, while the shape of the PDFs suggests any value of the  
 285 correlation length would be equally acceptable, even if large values ( $> 5$  km) are  
 286 favoured. The stability of the chains, shown in panels a–c in Figs. S1 and S2,

287 together with the ensemble of synthetic envelopes on panels j–q, indicate that all  
288 these models provide similarly good fits to the data and have similar loglikelihoods.  
289 This observation points to solutions being highly non-unique, and to the scattering  
290 parameters of the weakly heterogeneous layer not being easily recoverable for these  
291 high contrast cases.

292 Finally, model 5 contains three layers, with boundaries corresponding to upper  
293 and lower crust and lithospheric mantle. Our results are shown in Figs. 4 and  
294 Table 2. Chains converged in less than 130000 iterations. In all cases, PDFs  
295 are clearly non-Gaussian (panels d-l on Fig. 4) and have complex shapes, which  
296 widens the 5–95 PR and increases the range of suitable values of the parameters.  
297 The correlation length PDFs show clearly defined maxima near the true values of  
298 the parameter in all layers (the maximum distance between the maximum and the  
299 input parameter value being 0.35%). RMS velocity fluctuations PDFs are more  
300 complex and neither of them show clear maxima near the input parameter values.  
301 Figure S3 contains the marginal PDFs for all parameters in all layers, as well  
302 as the PDF for each individual parameter. It shows a strong trade-off between  
303 parameter values in different layers of the model, especially the two crustal layers,  
304 and allows us to identify two independent sets of parameters from our results (see  
305 Section S.1 in the Supplementary Material for details). This interaction between  
306 the parameters is caused by two main factors: first, the energy balance the EFMD  
307 is based on (Eq. 7) is strongly dependent on the layering of the model, since  
308 the maximum energy that can be present within a layer at any time depends on  
309 its thickness (i.e. energy leaks out of thinner layers faster); second, correlation  
310 length values have a much smaller effect on coda amplitudes, compared with RMS  
311 velocity fluctuations, so the algorithm uses  $\epsilon$  to compensate the excess or lack of  
312 energy within a layer and match data coda amplitudes. Since panels m–t on Fig.

313 4 do not show two clearly different sets of envelopes in our ensemble of synthetic  
314 envelopes, and given that the loglikelihood values remained stable throughout the  
315 three independent chains we ran for this example, we conclude that both sets of  
316 parameters we obtained from our inversion provide equally good fits to the data,  
317 even if neither of them match our input parameter values.

318 Overall, our results show that our Bayesian algorithm is capable of successfully  
319 fitting our data and retrieving the input parameter values for our 1-layer and 2-  
320 layer models. For our 3-layer model, however, the method provides good fits  
321 to the data but fails to obtain the correct parameter values, so we cannot trust  
322 results from this model for real data inversions, since we do not know what the  
323 scattering parameters are beforehand. Our observations illustrate the usefulness  
324 of the Bayesian approach we took in this study. It provides detailed information  
325 about the parameter space and indicates whether a single set of parameters that fits  
326 our data exists or a range of models can equally match the data. Any estimation  
327 of scattering parameters in a maximum-likelihood framework would therefore have  
328 led to erroneous conclusions about the physical parameters in this system, which  
329 we have avoided. The joint PDFs highlight the complicated relationships and  
330 trade-offs between the model parameters in the different settings explored here,  
331 which had not been observed in previous studies using the EFMD. We do not  
332 observe systematic overestimation of  $a$  in the EFMD, as reported by Hock et al.  
333 (2004). This observation might be related to the limited number of models tested  
334 in grid search approaches and the observed trade-offs between parameters.

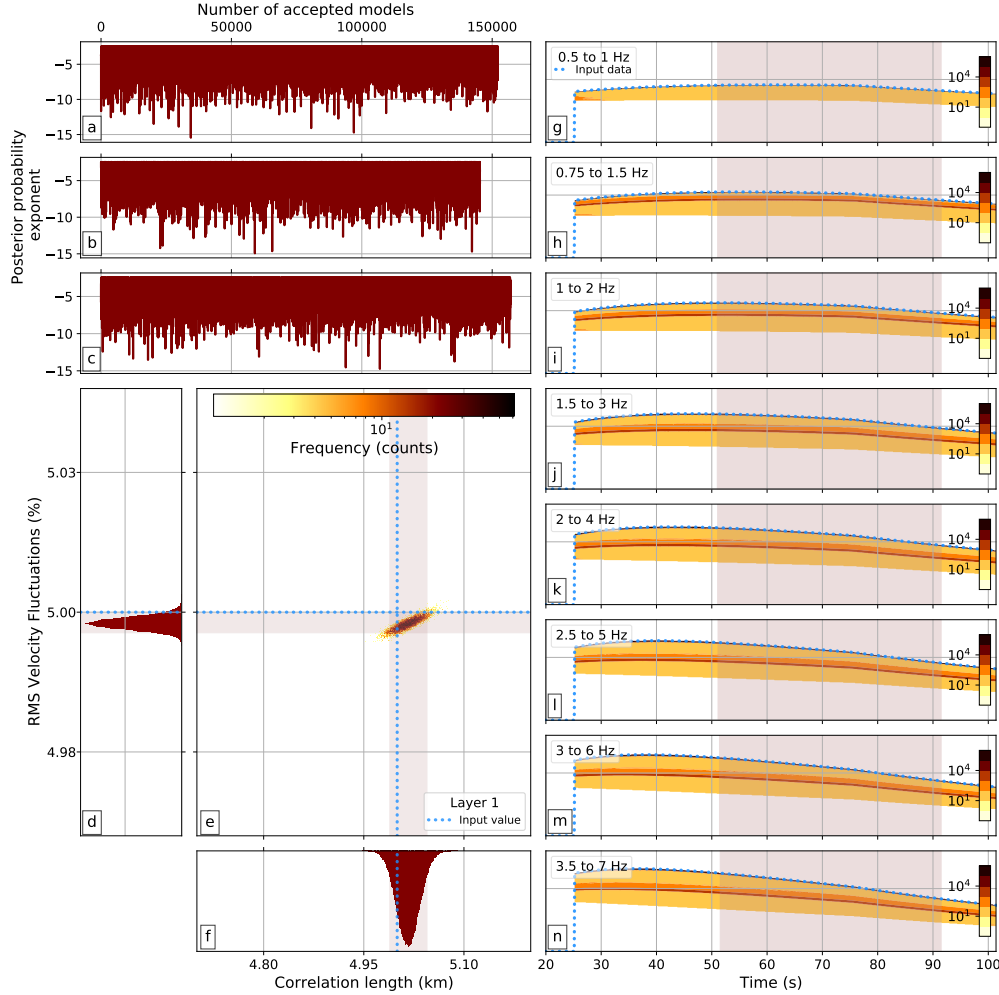


Figure 2: Summary of the results obtained from our EFMD algorithm for synthetic model 1 from Table 2 from three separate chains, adding up to a total of 3 million iterations (parameter combinations tested). Panels a–c show the loglikelihood (or posterior probability exponent) for each accepted model in the chain, once the burn-in phase was removed. Panels d–f contain the posterior PDFs of the structural parameters, as well as the joint PDF. Dotted blue lines in these plots represent the input parameter values and the shaded area corresponds to the 5–95 percentile range (PR). Panels g–n on the right show 2D histograms of the synthetic envelopes for all accepted models and frequency bands, with color bars indicating the number of models that produced a data sample within each bin. Vertical scale is the same in all plots. The shaded area here indicates the time window used for the fitting and blue dotted lines are the input data.

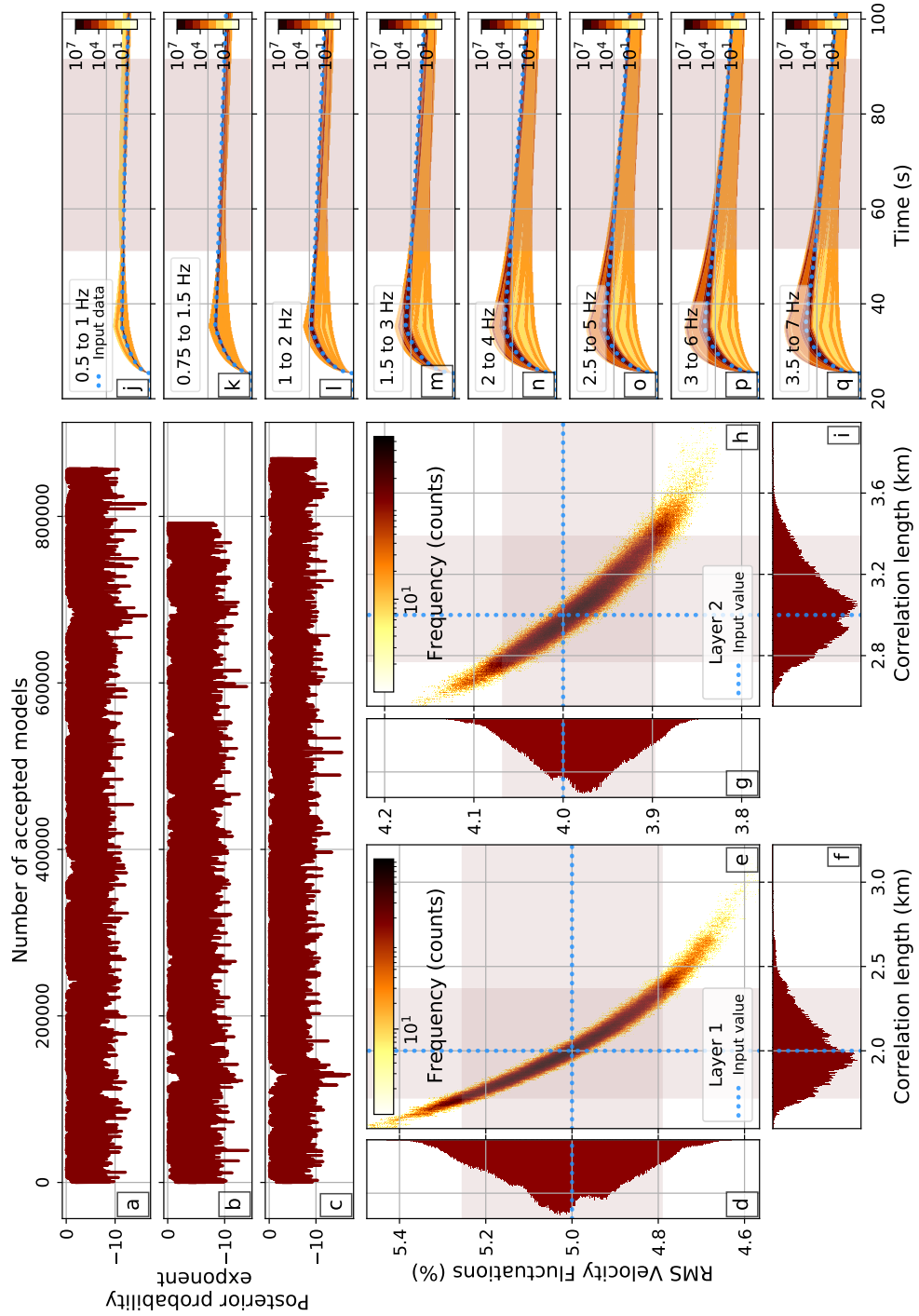


Figure 3: As Fig. 2 but for synthetic model 2 from Table 2 (2-layer model).

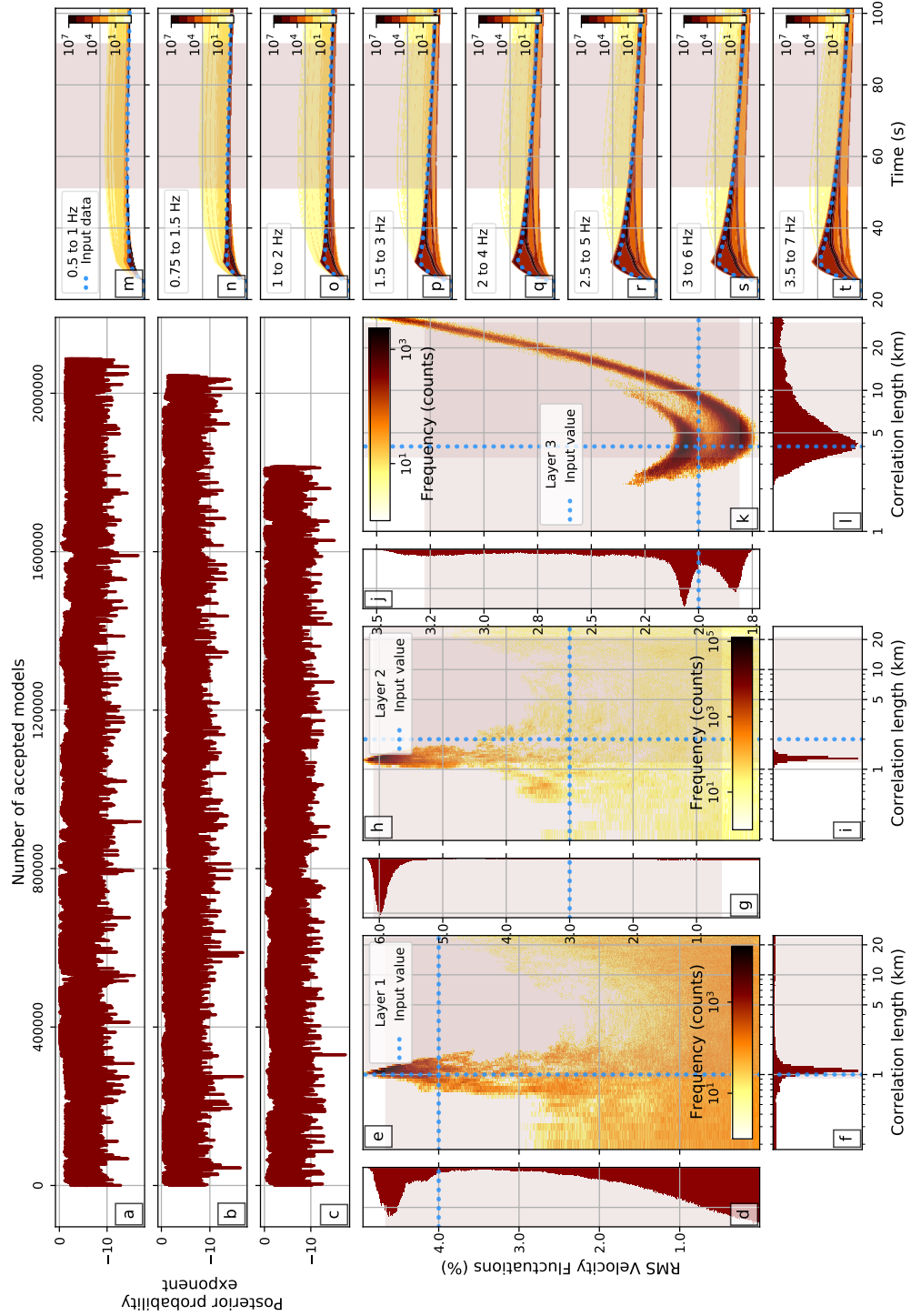


Figure 4: As Fig. 2 but for synthetic model 5 from Table 2 (3-layer model).

**Table 3:** Number of events and good quality (SNR > 5) traces for each array and frequency band.

		Number of events per frequency band							
		0.5–1 Hz	0.75–1.5 Hz	1–2 Hz	1.5–3 Hz	2–4 Hz	2.5–5 Hz	3–6 Hz	3.5–7 Hz
PSA	Events	86	161	213	276	343	268	212	158
	Traces	973	1899	2489	3226	3179	2965	2282	1641
WRA	Events	292	355	385	407	413	410	412	406
	Traces	709	843	916	977	983	984	980	965
ASAR	Events	309	375	440	429	405	397	386	374
	Traces								

### 335 3 DATA SELECTION AND PROCESSING

336 Our dataset consists of seismic recordings from teleseismic events from January  
 337 1, 2012 to December 31, 2018, and with epicentral distances between 30 and 80  
 338 degrees from the arrays, with source depths greater than 200 km and magnitudes  
 339 from 5 to 7. These conditions ensure vertical or nearly vertical incidence angles and  
 340 prevent near-source scattering and unwanted deep seismic phases from appearing  
 341 in our time window of interest.

342 After removing the instrument response, we calculate the signal-to-noise ratio  
 343 (SNR) for each trace and frequency band using the peak-to-peak amplitude in two  
 344 separate time windows: for noise, we used a 20 s long window, starting  $\sim 25$  s  
 345 before the theoretical P-wave arrival (as estimated from PREM (Dziewonski and  
 346 Anderson, 1981)), while for the signal we chose a time window starting 1 second  
 347 before the theoretical first arrival and ending 40 seconds later. Only traces with  
 348 signal-to-noise ratio equal to or higher than 5 were used.

349 Hock et al. (2004) pointed out that the EFMD generally overestimated the  
 350 RMS velocity fluctuations by up to 3% when using only vertical-component data  
 351 and that a mix of 1-component and 3-component data produced unstable results,  
 352 both of them caused by the difference in coda amplitudes between 1-component and  
 353 3-component data. However, the IMS arrays are dominantly vertical component,

354 with WRA having three 3-component stations and ASAR a single 3-component  
355 central station. All PSA stations are three-component. To address this issue, we  
356 tried calculating a correction factor to approximate 1-component to 3-component  
357 coda levels. We used several different approaches to obtain this correction factor,  
358 all of them based on the ratio between every available 3-component coda envelope  
359  $A(t; \omega_c)$  or normalised envelope (left hand side on Eq. 5) and its 1-component (ver-  
360 tical) counterpart. However, we found that these ratios varied significantly from  
361 event to event and frequency band to frequency band and followed complicated  
362 probability distributions, even after using our large datasets to calculate them. The  
363 corrected 1-component envelopes did not in general fully match the 3-component  
364 coda amplitudes using this approach. Our tests also showed the correction fac-  
365 tors needed for the normalised envelopes were different than for the unnormalised  
366 ones and that small variations in coda amplitudes affected the results we got from  
367 both the EFM and EFMD. We also used the “corrected” 1-component data in our  
368 EFM-EFMD algorithm and compared the results in different settings with those  
369 from our 3-component data for PSA. In both cases, the distribution of the het-  
370 erogeneity followed similar patterns, but the values of the scattering parameters  
371 and the posterior PDFs differed. Therefore, we only analyse 3-component data  
372 in this study. Table 3 shows the number of events and traces used for each array  
373 and frequency band. For PSA, we only kept events with 5 or more good quality 3-  
374 component traces. For WRA and ASAR, we used all available 3-component data.  
375 This allowed us to test this method with different station configurations, from  
376 a full array (PSA) to a small group of stations (WRA) or even a single station  
377 (ASAR). In all cases, our large event dataset guarantees a thorough sampling of  
378 the structure beneath the stations and allows us to obtain robust results.

379 For each array, the data processing prior to the EFM/EFMD analysis was

380 carried out as follows:

381 (i) Computation of 3-component envelopes for each frequency band, station and  
 382 event. All traces were trimmed to the time window going from  $t_N$  seconds  
 383 before to  $3t_N$  seconds after the theoretical P wave arrival ( $t_N$  being the travel  
 384 time through the lithosphere,  $\sim 25$  s for all arrays). These were then stacked  
 385 by event, normalised using Eq. 5 and stacked by frequency band. Unnor-  
 386 malised envelopes for all events were also stacked by event and frequency  
 387 band. The variance of both normalised and unnormalised envelopes was cal-  
 388 culated sample by sample from all individual event stacked envelopes and  
 389 used as the uncertainty of our data.

390 (ii) Estimation of  $Q_s$ ,  $Q_i$ ,  $Q_{diff}$ ,  $a$  and  $\epsilon$  for a single scattering layer using the  
 391 EFM.

392 (iii) Bayesian inversion for the structural parameters of each layer in each model  
 393 type from Fig. 5 by applying the envelope modelling technique from EFMD,  
 394 as described in Section 2.2, and using the  $Q_i$  values obtained from the single  
 395 layer EFM. In order to speed up this process, our data were resampled to a  
 396 common sampling rate of 10 Hz (original sampling rates were 40 Hz for PSA  
 397 and WRA and 20 Hz for ASAR) before applying the EFMD algorithm.

398 Background lithospheric P-wave velocities for each seismic array were ob-  
 399 tained from the Australian Seismological Reference Model (AuSREM; Kennett  
 400 and Salmon (e.g., 2012); Salmon et al. (e.g., 2013b); Kennett et al. (e.g., 2013);  
 401 Salmon et al. (e.g., 2013a) (Fig. 5).

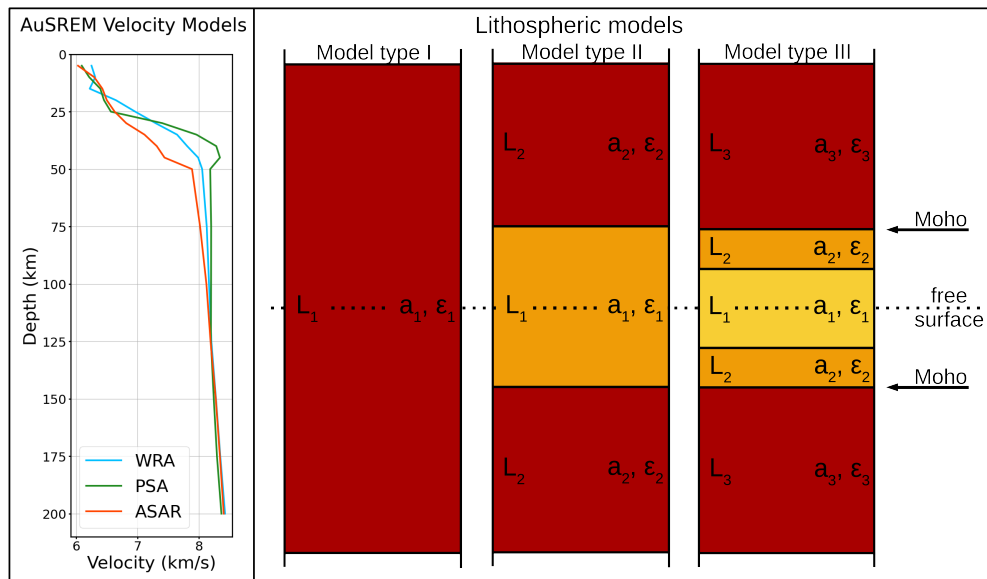


Figure 5: Representation of the AuSREM P-wave velocity models for each seismic array (left) and the three types of lithospheric models used in the EFMD (right). The layering is the same we used in the models for our synthetic tests, with Model types I, II and III corresponding to Models 1, 2 and 5 from Table 2 (Models 2, 3 and 4 have the same layering).

402 **4 TECTONIC SETTING**

403 ASAR and WRA are located on the North Australian Craton (NAC), one of the  
404 Proterozoic cratons in the Precambrian westernmost two-thirds of the Australian  
405 continent (e.g. Myers, 1990; Simons et al., 1999; Cawood and Korsch, 2008; Well-  
406 man, 1998) (Fig. 6). The NAC consists of late Archaean to Proterozoic cratonic  
407 blocks overlaid by Proterozoic and Phanerozoic orogenic belts and basins. PSA  
408 is located on Archaean lithosphere part of the West Australian Craton (WAC),  
409 which includes both the Pilbara and Yilgarn Archaean cratons, as well as some  
410 Proterozoic orogens and basins (Cawood and Korsch, 2008) (Fig. 6). Present day  
411 tectonic activity in Australia is concentrated along the active plate boundaries in  
412 the north and east, with continental regions presenting only moderate seismicity  
413 (Fichtner et al., 2009).

414 Previous studies have investigated crust and lithospheric thicknesses and struc-  
415 ture around the three arrays studied here. Thick crust ( $L_c > 40$  km) with a wide  
416 and smooth Moho transition has generally been found in the Proterozoic shields  
417 of Central Australia while the Archaean regions of western Australia have thinner  
418 crust ( $L_c < 40$  km) and sharper crust-upper mantle transitions (e.g. Clitheroe  
419 et al., 2000; Sippl, 2016; Salmon et al., 2013a; Kennett et al., 2011; Kennett and  
420 Saygin, 2015). This difference in crustal thickness between Archaean and Pro-  
421 terozoic regions seems not to fit the trend of crustal thickness increasing with age  
422 suggested for Australia (e.g. Clitheroe et al., 2000). It has been attributed to post  
423 Archaean tectonic activity underplating material at the base of the crust in these  
424 regions, as opposed to the Archaean cratons being located at passive margins and,  
425 therefore, not being affected by more recent tectonics (e.g. Drummond and Collins,  
426 1986).

427 Sippl (2016) and Kennett and Sippl (2018) imaged a series of Moho offsets

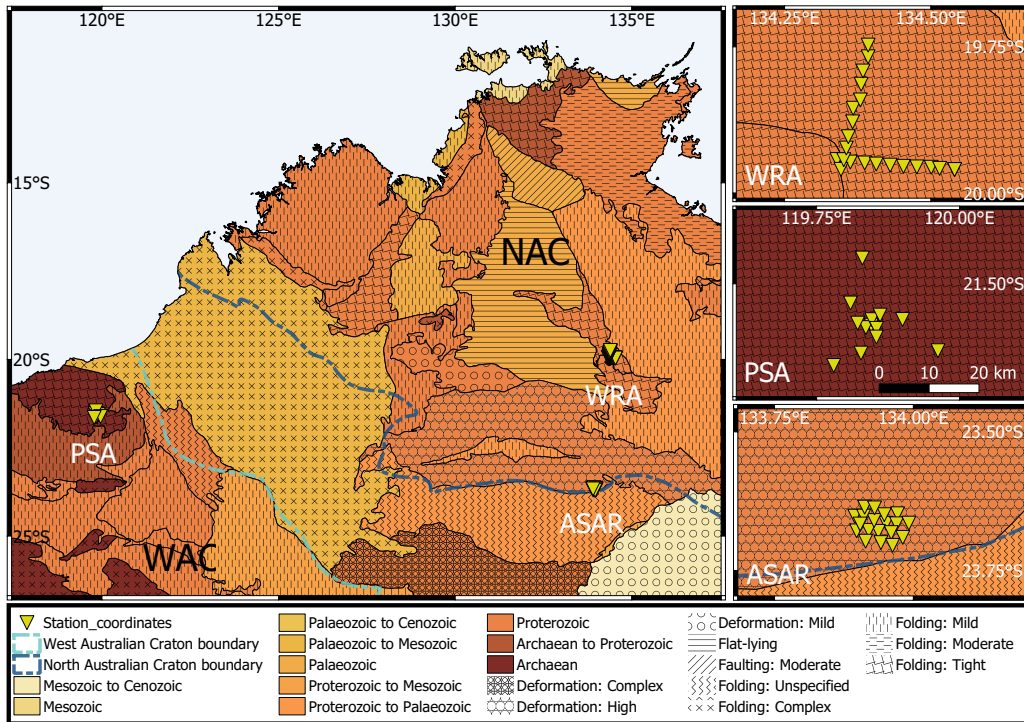


Figure 6: Simplified geological map of northwestern Australia and location of the three seismic arrays used in this study (Alice Springs Array (ASAR), Warramunga Array (WRA) and Pilbara Seismic Array (PSA)). Blue dashed lines represent the boundary of the West Australian Craton (WAC, light blue line) and the North Australian Craton (NAC, dark blue line). PSA and WRA are located on Archaeal and Proterozoic basement respectively, inside the cratons, while ASAR is situated at the southern boundary of the NAC. Panels on the right show the station configuration of the arrays, with the same scale bar shown for PSA being applicable to all three maps. Geological structure based on Blake and Kilgour (1998) and Raymond et al. (2018).

428 along a north-south profile in the NAC. One of these offsets is associated with the  
 429 Redbank Shear Zone, which separates the Aileron Province and the location of  
 430 ASAR from the Amadeus Basin, just south of the array (e.g Goleby et al., 1989;  
 431 Korsch et al., 1998; Sippl, 2016). The profile used in Sippl (2016) and Kennett  
 432 and Sippl (2018) is located roughly 50 km west of ASAR and shows an offset  
 433 of up to 20 km coinciding with ASAR latitude, even though they show constant  
 434 Moho depths beneath the array. An east-west gravity anomaly has been found

435 at the location of this Moho offset (Sipl, 2016, Fig. 1) and attributed to denser  
 436 lithosphere at the base of the crust caused by the uplift of the Aileron crustal block  
 437 during the Alice Springs Orogeny 400-350 Ma ago (Goleby et al., 1989; Aitken,  
 438 2009; Aitken et al., 2009; Sipl, 2016). This observation seems to conflict with the  
 439 AusMoho model (Kennett et al., 2011, Fig. 6), which shows stable Moho depths  
 440 in this part of the profile, with a slight ( $\sim 2$  km) north-south depth decrease at the  
 441 ASAR location. The lower resolution of the AusMoho model may be the reason  
 442 for this difference. Another offset imaged by Sipl (2016) and Kennett and Sipl  
 443 (2018), further north, shows a north-south decrease in Moho depth of about 10 km  
 444 just south from WRA, which has been associated with a Proterozoic suture zone.  
 445 Corbishley (1970) also found evidence of a layered and dipping structure below  
 446 WRA. Gravimetric data do not show any anomalies here (Sipl, 2016), which has  
 447 been attributed to a layer of sediments near the surface isostatically compensating  
 448 the mass excess at depth. In this case the AusMoho model does show a sharp ( $\sim 7$   
 449 km) north-south decrease in Moho depth around this location.

450 Several studies have addressed the thickness of the lithosphere in the Australian  
 451 continent. Some suggest similarly deep interfaces across all Precambrian cratonic  
 452 regions in Australia ( $L_l \approx 200$  km) (e.g. Debayle and Kennett, 2000). More  
 453 recent studies use a lithosphere-asthenosphere transition zone (LAT), defined as a  
 454 mechanical or thermal boundary layer related to changes in rheology, as opposed  
 455 to a simple interface at the bottom of the lithosphere (e.g. Kennett and Sipl,  
 456 2018; Yoshizawa and Kennett, 2015). Specifically, Kennett and Sipl (2018) place  
 457 the upper and lower bounds of the LAT at 140 and 170 km depth respectively  
 458 for ASAR, and at 120 and 160 km for WRA, while Yoshizawa and Kennett (2015)  
 459 place them at 100 and 200 km depth for PSA. Some studies have also found  
 460 evidence for mid-lithospheric discontinuities below both ASAR and WRA, at 90

461 and 91 km respectively (e.g. Ford et al., 2010; Kennett and Saygin, 2015; Kennett  
462 et al., 2017).

**Table 4:** Summary of the main results obtained from the EFM for all arrays: intrinsic ( $Q_{i0}$ ) and diffusion ( $Q_{d0}$ ) quality factors values at 1 Hz, intrinsic quality factor frequency dependence coefficient ( $\alpha$ ), correlation length ( $a$ ) and RMS velocity fluctuations ( $\epsilon$ ).

Array	$Q_{i0}$	$Q_{d0}$	$\alpha$	$a$ (km)	$\epsilon$ (%)
PSA	$2100 \pm 200$	$500 \pm 40$	0.0	$0.9 \pm 0.1$	$2.9 \pm 0.1$
WRA	$2100 \pm 100$	$400 \pm 20$	0.0	$1.1 \pm 0.1$	$4.5 \pm 0.1$
ASAR	$1000 \pm 100$	$400 \pm 40$	0.2	$0.9 \pm 0.2$	$4.7 \pm 0.2$

## 463 5 RESULTS AND DISCUSSION

### 464 5.1 EFM results

465 We calculated the coda decay rate,  $a_1$ , and its value at zero time,  $a_0$ , for all  
 466 frequency bands and arrays as stated in Section 2.1. We applied the linear least-  
 467 squares fit of the squared stacked envelopes at the free surface (Fig. S4) to a time  
 468 window starting  $t_N$  s after the theoretical P wave arrival ( $t_N$  being the one-way  
 469 travelttime through the lithosphere), since the EFM is only applicable after the  
 470 direct wave has left the scattering layer (Korn, 1990; Hock and Korn, 2000). The  
 471 length of this time window varied from 42.5 to 48 s for all arrays and frequency  
 472 bands, depending on differences in P wave velocities and arrival times. Table 4  
 473 and Figure 7 summarise our EFM results for all arrays.

474 A least-squares fit using Eq. 2 then allowed us to calculate the quality factors  
 475 for diffusion and anelasticity at 1 Hz from  $a_1$ . For all arrays, the coda decay rate for  
 476 the lowest frequency band did not follow the trend defined by the other frequency  
 477 bands. Including it in the least squares fit produced inconsistent results, and it  
 478 was excluded from the analysis (Fig. S5). The intrinsic quality factor,  $Q_i$ , takes  
 479 similar, frequency independent ( $\alpha = 0$ ), values of  $\sim 2000$  for WRA and PSA. For  
 480 ASAR, our best fits to the coda decay rate (Eq. 2) correspond to  $\alpha = 0.2$  (Fig.  
 481 S5) and  $Q_i \sim 1000$ . Diffusion quality factor values at 1 Hz are similar for ASAR

482 and WRA ( $\sim 400$ ), and higher for PSA ( $\sim 500$ ). Since this quality factor does not  
 483 depend on  $\alpha$  (Eq. 16, Korn (1990)), this translates into  $Q_{diff}$  following the same  
 484 trend for all arrays but being higher for PSA than for WRA and ASAR.

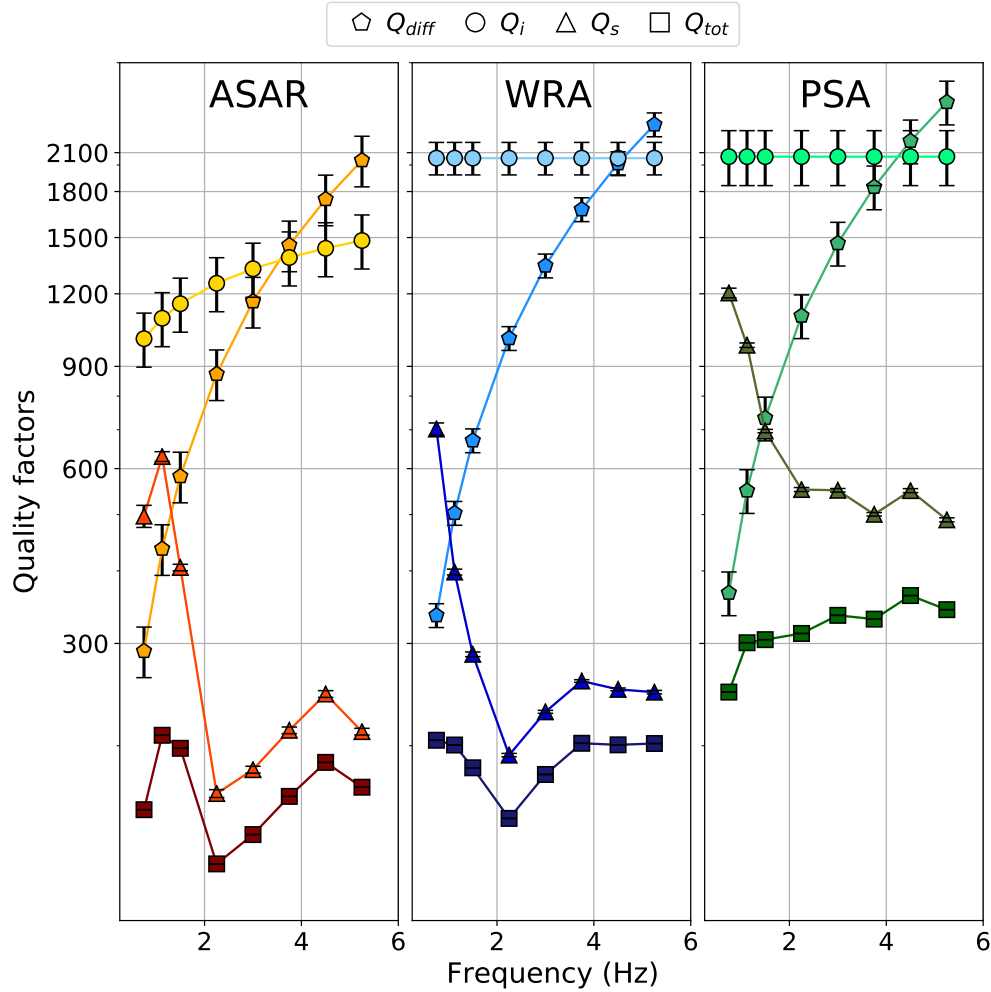


Figure 7: Frequency dependence of the intrinsic ( $Q_i$ ), the diffusion ( $Q_{diff}$ ), scattering ( $Q_s$ ) and total ( $Q_{tot}$ ) quality factors for all arrays.

485 Despite the possibility to determine the type of ACF of the scattering structure  
 486 using the EFM, we assumed an exponential ACF based on the similarity between  
 487 different ACFs within our frequency range of interest and previous studies which

488 have proposed it as an appropriate ACF for teleseismic scattering studies (Shearer  
 489 and Earle, 2004). Figure S6 shows measured  $Q_s$  values, obtained from Eq. 3,  
 490 together with the theoretical least-squares regression curves derived by Fang and  
 491 Müller (1996) for the relationship between the structural parameters and  $Q_s$  for  
 492 an exponential ACF. The total quality factor,  $Q_{tot}$ , and  $Q_s$  follow a similar trend.  
 493 They take the highest and lowest values for PSA and ASAR respectively. For  
 494 WRA and ASAR, their maximum value corresponds to the 0.5–1 and 0.75–1.5  
 495 Hz bands respectively, and the minimum for the 1.5–3 Hz frequency band. The  
 496 frequency dependence of  $Q_s$  and  $Q_{tot}$  for the highest frequencies is similar for both  
 497 arrays. This indicates that the dominating scale length of the heterogeneity is in  
 498 the 2.6–5.3 km range for these arrays when we consider a single scattering layer.  
 499 For PSA, however,  $Q_s$  decreases for frequencies below 1.5 Hz and then remains  
 500 approximately constant, which could be indicative of different scale lengths of the  
 501 heterogeneity being equally present in the structure. For this array,  $Q_{tot}$  increases  
 502 slowly over the frequency range covered here.

503 In general, diffusion is the strongest attenuation mechanism (lowest Q) at low  
 504 frequencies, with scattering dominating at higher frequencies. For WRA, this  
 505 transition happens at 0.75 Hz, while for ASAR and PSA, the change takes place  
 506 at 1.125 Hz. Anelasticity remains the weakest attenuation mechanism (highest Q)  
 507 at low frequencies, up to 4.5 Hz for WRA and PSA and 3.75 Hz for ASAR. Above  
 508 that frequency,  $Q_{diff}$  becomes dominant. These results agree with the observations  
 509 by Korn (1990), who obtained  $Q_i > 1000$  and  $Q_{diff} \sim 300 - 400$  at 1 Hz for WRA,  
 510 even if his results showed that  $Q_i$  remained larger than  $Q_{diff}$  up to 10 Hz. Our  
 511  $Q_{tot}$  results suggest that, even if  $Q_s$ ,  $Q_i$  and  $Q_{diff}$  are lower at most frequencies for  
 512 ASAR than for the other two arrays, total attenuation strength is similar for ASAR  
 513 and WRA. These lower  $Q_{tot}$  values could be related to the location of these arrays

514 on the NAC, younger in origin than the WAC (Section 4). The location of ASAR,  
 515 on the southern edge of the NAC, in an area widely affected by the accretionary  
 516 processes that took place during the assembly of the Australian continent, as well  
 517 as major events like the Petermann and Alice Springs orogens (Section 4), could  
 518 explain the lower values of the different quality factors obtained for this array.  
 519 For PSA, the generally high quality factors values we obtained could be related  
 520 to the location of the array on a tectonically quiet Archaean craton (Section 4).  
 521 Previous studies (e.g. Cormier, 1982; Korn, 1993; Sipkin and Revenaugh, 1994;  
 522 Domínguez and Rebollar, 1997) have also found lower  $Q$  values in regions with  
 523 quiet tectonic histories, an observation that matches our results from the EFM for  
 524 all three arrays.

## 525 **5.2 EFMD results**

526 We used the 1-layer and 2-layer lithospheric models shown in Fig. 5 in our inversion  
 527 of the data for all three arrays.  $Q_i$  values necessary to calculate the synthetic  
 528 envelopes from Eq. 5 are determined by the EFM. As with our synthetic tests,  
 529 we ran three parallel Markov chains for each array and model type, with 1 million  
 530 or 3 million iterations for models with 1 and 2 layers respectively. The burn-in  
 531 phase, defined as described in section 2.2.2, was removed from all chains. Table 5  
 532 summarises our results. To avoid repetition, we include here only the most relevant  
 533 results for each array. Figures from the rest of our inversions can be found in the  
 534 Supplementary material.

535 Inversion of PSA data with Model type I (single layer), revealed this model  
 536 produces very large amplitude codas that barely decay over time (Fig. S7). All  
 537 chains were stable and converged within 14000 iterations, but the maximum log-  
 538 likelihood reached during the inversion ( $< -10^6$ , panels a-c on Fig. S7), indicated

539 fits to the data are very poor, which is also obvious from the comparison of the  
 540 ensemble of synthetic envelopes with the data (panels g–n on Fig. S7). The poste-  
 541 rior PDFs suggest a nearly homogeneous lithosphere, with  $\epsilon \sim 0\%$  and  $a > 20$  km.  
 542 This is likely due to the large thickness of the layer (200 km) preventing diffusion  
 543 out of it and, therefore, energy levels in the heterogeneous layer remaining high at  
 544 all times, regardless of the magnitude of the scattering parameters. We also tested  
 545 model type I on ASAR data, since coda levels for this array are higher. These  
 546 results are shown on Fig. S8. Despite the higher coda amplitudes, model type I  
 547 fails to fit our data for this array, with the maximum loglikelihood reached being  
 548 on the order of  $-10000$ . ASAR coda amplitudes are similar to WRA, indicating  
 549 similar behaviour. Therefore, this model was not tested for WRA.

550 Model type II (two layer) inversions for all three arrays showed much better  
 551 fits for frequency bands D-H (Table 1) than for A-C (example for PSA in Fig.  
 552 S9). However, loglikelihood values are still very low ( $< -4 \times 10^5$ ), Table 5), which  
 553 indicates poor fits to the data and, therefore, unreliable parameter estimations,  
 554 even if there is a substantial improvement with respect to model type I. Our EFM  
 555 results show scattering only becomes the dominant attenuation mechanism above  
 556 1.5 Hz for PSA (Fig. 7). This, together with coda amplitudes shown on panels  
 557 j–q in Fig. S9 being barely above the noise level in the time window of interest  
 558 for the lowest frequency bands, suggests these codas are affected by large-scale  
 559 heterogeneities and might not be composed only of energy scattered at small-scale  
 560 structure. Therefore, the EFMD may not be able to fit our coda envelopes for  
 561 frequencies below this threshold. To test this, we ran our EFMD inversion code  
 562 for frequency bands D to H (Table 1) alone. By comparing our results for PSA  
 563 in Fig. S9 and Fig. 8, we observe considerable improvement in the fits to the  
 564 data, also evidenced by much higher loglikelihood values ( $< -10$ ). Given these

**Table 5:** Summary of our EFMD results for all arrays and model types.

Array	Model type	Frequency bands	Layer number	Correlation length ( $a$ )		RMS velocity fluctuations ( $\epsilon$ )		Maximum $L$
				5-95 PR (km)	AR (%)	5-95 PR (%)	AR (%)	
PSA 3 comp.	I	A-H	1	23 - 32	48	< 0.01	47	< $-14 \times 10^6$
	II	A-H	1	0.5 - 25	75	< 0.01	47	< -450000
			2	0.5 - 32		< 0.01		
	II	D-H	1	0.5 - 0.8	59	2.3 - 2.5	44	-7.1
2			4 - 32	0.1 - 1.8				
ASAR	I	A-H	1	2 - 30	93	0.01 - 0.07	44	-10500
	II	D-H	1	0.2 - 1.4	59	2.4 - 3.0	50	-2.2
2			3 - 32	0.1 - 3.7				
WRA	II	D-H	1	0.7 - 1.5	60	3.1 - 3.9	53	-0.7
			2	3 - 32		0.2 - 5.0		

565 new observations, we discard frequency bands A to C (central frequencies below  
566 1.5 Hz, Table 1) in future inversions of the data for all arrays.

567 Figures 8, 9 and 10 summarise our results for all three arrays and model type  
568 II. All Markov chains converged within 10000, 7000 and 4000 iterations for PSA,  
569 ASAR and WRA, respectively. The scattering structure beneath all three arrays  
570 shows different amounts of heterogeneity in the crust and a relatively homogeneous  
571 lithospheric mantle. The posterior PDFs for both parameters in the top layer in  
572 all cases are roughly Gaussian and narrow (Table 5). Maxima for the correlation  
573 length PDFs for PSA, ASAR and WRA are at 0.6, 0.7 and 1 km, while RMS  
574 velocity fluctuations posteriors peak at 2.4%, 2.7% and 3.6% respectively. PDFs  
575 for layer 2, on the other hand, show no clear maxima and also have similar shapes  
576 for all arrays. For PSA,  $\epsilon$  only takes values below  $\sim 3\%$ , while for WRA and  
577 ASAR, the PDF extends up to  $\sim 8\%$  and  $\sim 6\%$  respectively. In all cases, most of  
578 the accepted models have  $\epsilon < 1\%$ . The correlation length PDF, on the other hand,  
579 extends throughout the entire parameter space. For PSA and WRA, large values  
580 of  $a$  ( $> 5$  km) are favoured, while small correlation lengths ( $< 1$  km) seem to  
581 work better for ASAR. Loglikelihood values are high ( $> -10$ ) for all arrays, which  
582 suggests fits to the data are generally good. The shape of the PDFs for the bottom  
583 layer makes our solutions non-unique and similar to our results for synthetic model

584 4, which had strong scattering in the crust and a fairly homogenous lithospheric  
 585 mantle. This would mean scattering takes place mostly in the crust for all three  
 586 arrays, with very weak or no scattering at all in the upper mantle. Finally, we  
 587 used the lower and higher ends of the 5–95 PR for each scattering parameter,  
 588 array and frequency band to calculate the minimum and maximum values of  $Q_s$   
 589 in each layer. The average scattering quality factor for the lithosphere can be  
 590 calculated from these values. Figure S10, in the Supplementary Material, shows  
 591 a comparison between our  $Q_s$  values from the EFM and the ones derived from  
 592 the EFMD scattering parameters. In all cases, the EFM  $Q_s$  values fall within the  
 593 calculated range of values for the EFMD.

594 These results agree with observations from previous studies. Kennett (2015)  
 595 studied P-wave reflectivity in the lithosphere and asthenosphere in Australia.  
 596 Their results point to strong lithospheric heterogeneity being present beneath sta-  
 597 tions in the Proterozoic NAC and they suggest correlation lengths of at most a  
 598 few kilometres and  $\sim 2\%$  velocity fluctuations in the crust. For the lithospheric  
 599 mantle, they propose much larger correlation lengths (10-20 km) and  $\epsilon < 1\%$ .  
 600 Kennett and Furumura (2016) and Kennett et al. (2017) also addressed the pres-  
 601 ence and interaction of multi-scale lithospheric heterogeneity in the Australian  
 602 continent. In their simulations, they combined large scale heterogeneities with  
 603 stochastic media and fine scale structure. Their results indicate a wide range of  
 604 heterogeneity spatial scales are present and interact within the lithosphere. Their  
 605 models contain four different layers for the fine scale structure, two in the crust  
 606 and two in the lithospheric mantle, and different horizontal ( $a_H$ ) and vertical ( $a_V$ )  
 607 correlation lengths. Their scattering parameters suggest a mildly heterogeneous  
 608 asthenospheric mantle ( $a_H = 10$  km,  $a_V = 10$  km,  $\epsilon = 0.5\%$ ) and an increase in  
 609 the strength of the heterogeneity in the lithosphere-asthenosphere transition zone

610 ( $a_H = 5$  km,  $a_V = 1$  km,  $\epsilon = 1$  %). The crust is generally more heterogeneous in  
 611 these models, with  $a_H = 2.6$  km,  $a_V = 0.4$  km for both crustal layers and RMS  
 612 velocity fluctuations of 0.5% and 1.5% for the upper and lower crust respectively.  
 613 At resolvable scales, these values are consistent with our results from the EFMD  
 614 (Table 5).

### 615 5.2.1 Limitations and assumptions

616 A possible source of error in our inversion is the prescribed thickness of the layers in  
 617 our models. The EFMD is sensitive to changes in the bottom depth of the different  
 618 layers, especially for the shallowest layer, as this affects the diffusion out of them.  
 619 For our model type II, we used a priori information on Moho and lithosphere-  
 620 asthenosphere boundary (LAB) depths. As discussed in Section 4, however, there  
 621 is some uncertainty in reported depths, especially for the LAB. Our inversion  
 622 considers the lithosphere to extend down to 200 km depth for all three arrays, but  
 623 tests of the EFMD with shallower LABs did not produce significant changes in  
 624 our results.

625 Other limitations of our approach are the assumptions for the determination  
 626 of the different quality factors in the EFM and the fact that neither the EFM nor  
 627 the EFMD take into account phase conversions and reflections at interfaces other  
 628 than the free surface. Equation 15b from Korn (1990), which we use in this study,  
 629 is based on the assumption that  $Q_s$  and  $Q_{diff}$  are of the same order of magnitude,  
 630 even if that is not necessarily always the case. The intrinsic quality factor ( $Q_i$ )  
 631 value used in the EFMD was determined by the EFM, with a limitation to a single  
 632 scattering layer and a poorly constrained frequency dependence of  $Q_i$ , since  $\alpha$   
 633 could not be fully inverted for in the EFM (Section 2.1). Therefore, all layers in  
 634 our EFMD models have the same  $Q_i$  and frequency dependence as obtained in the

635 EFM. The heterogeneity anisotropy observed by Kennett and Furumura (2016)  
636 and Kennett et al. (2017) could be included in future approaches of Bayesian  
637 inversion for heterogeneity structure but given the range of acceptable models  
638 we find and the trade-offs inherent in inverting for scattering parameters we have  
639 demonstrated, we are unsure if anisotropy in scattering could be well resolved with  
640 these kinds of data.

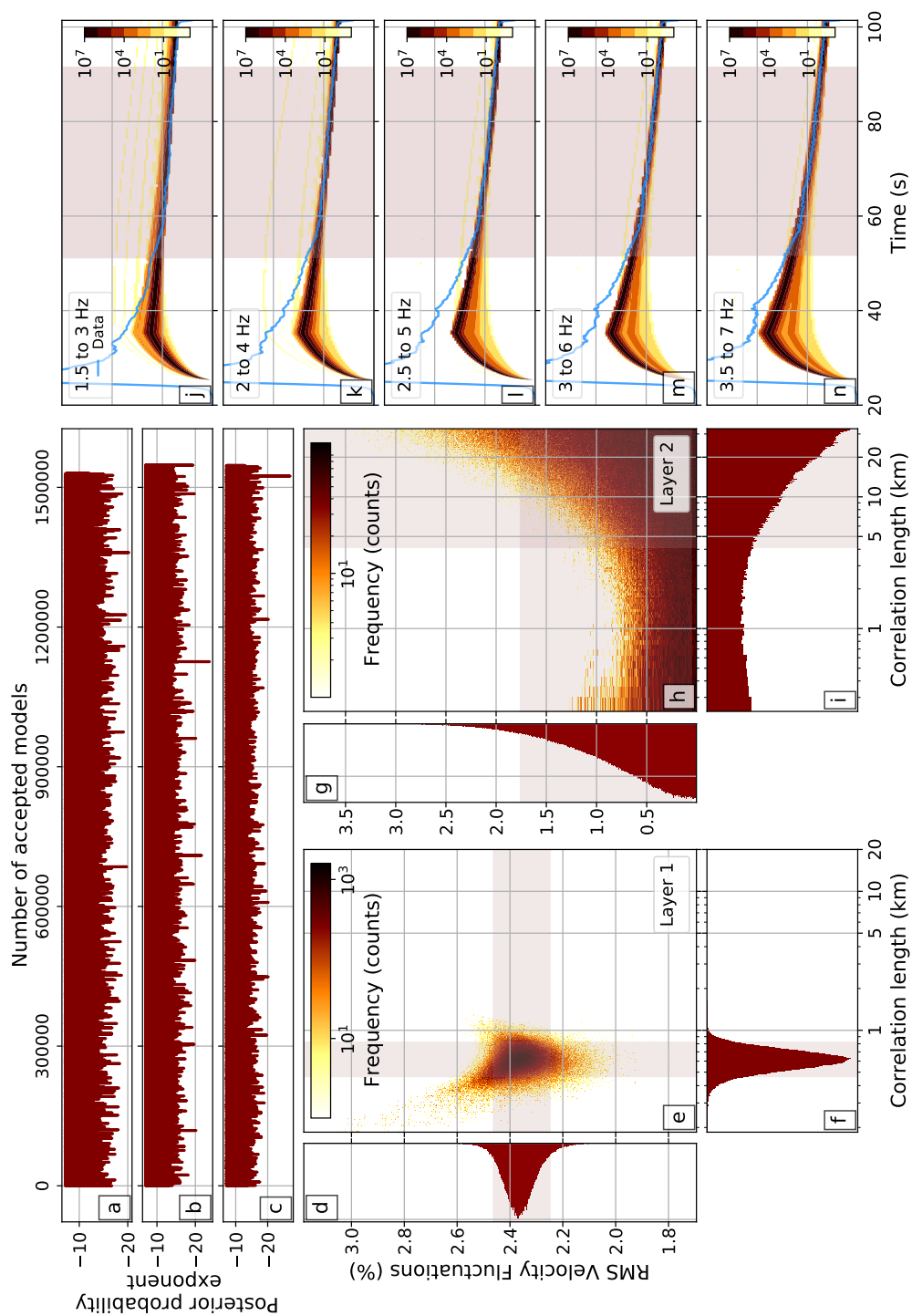


Figure 8: Results from Model type II and PSA using only the five highest frequency bands from Table 1.

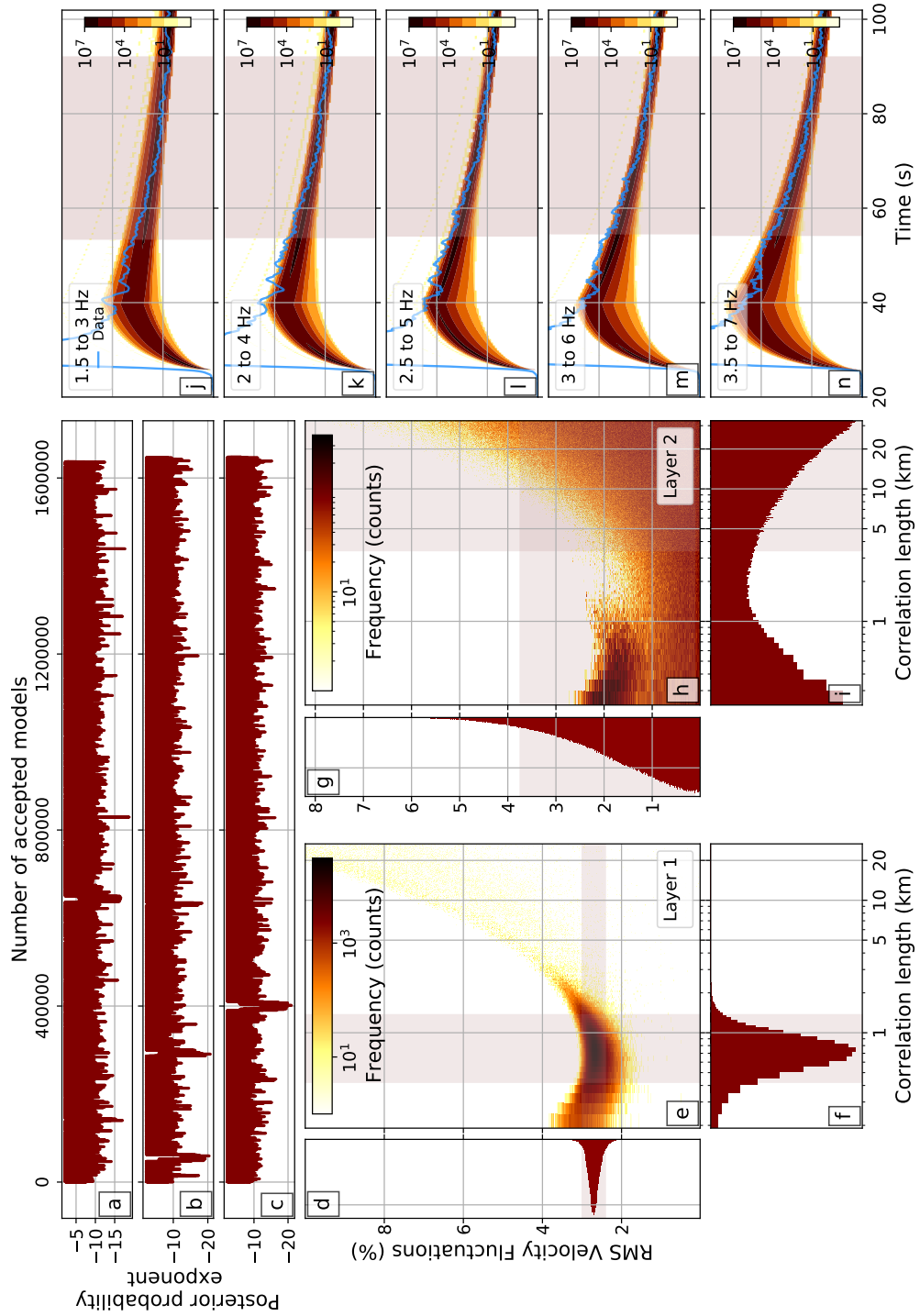


Figure 9: As Fig. 8 but for ASAR.

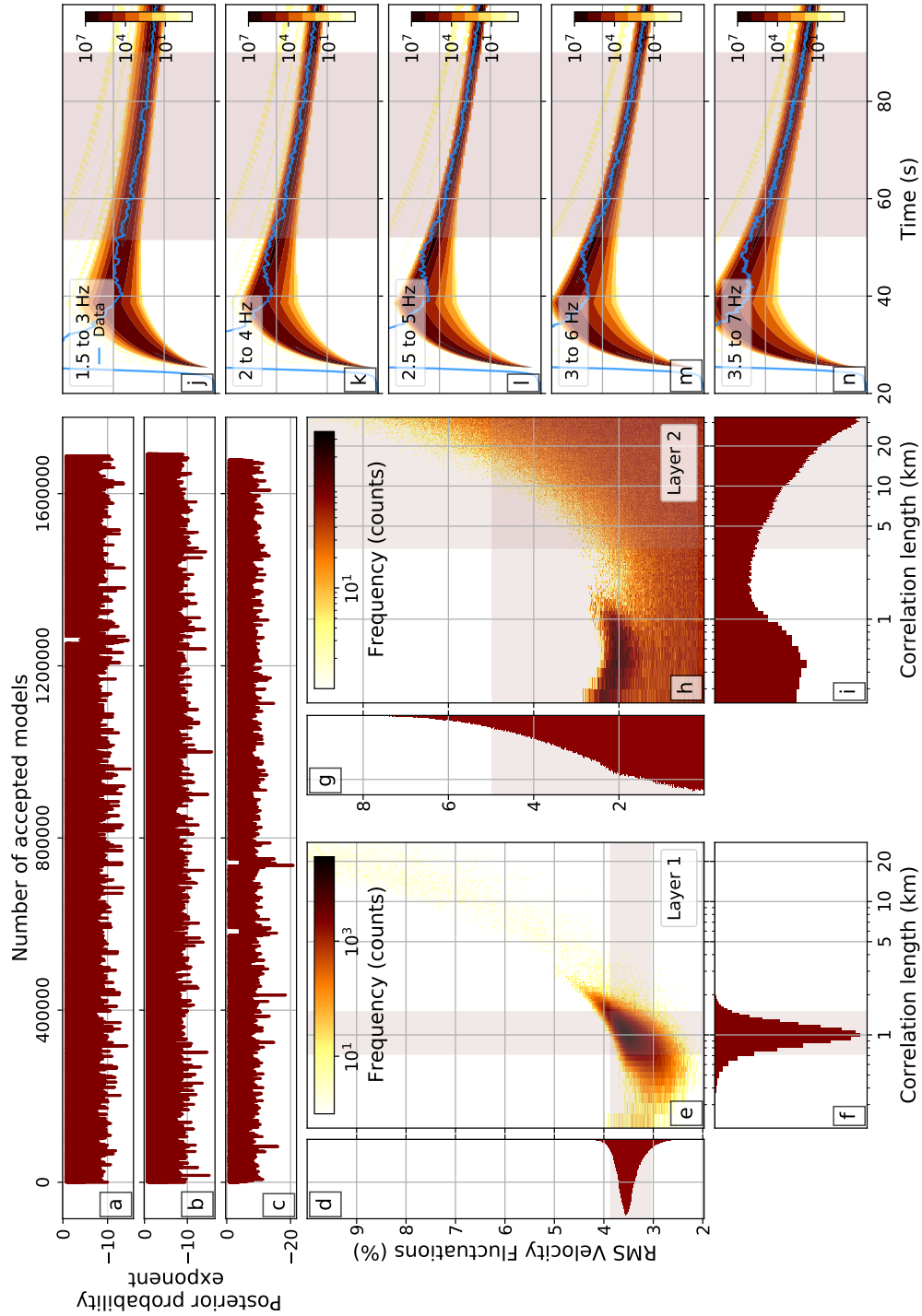


Figure 10: As Fig. 8 but for WRA.

641 **6 CONCLUSIONS**

642 For three Australian seismic arrays, we applied the single layer modified Energy  
643 Flux Model (EFM) and depth dependent Energy Flux Model (EFMD) to a large  
644 dataset which includes events from a wide range of magnitudes, distances and  
645 azimuths. This ensures we are thoroughly sampling the structure of the litho-  
646 sphere beneath the arrays and reduces azimuthal and lateral bias. Our EFM  
647 results highlight similarities and differences in the behaviour of the quality factors  
648 ( $Q_i$ ,  $Q_{diff}$ ,  $Q_s$ ,  $Q_{tot}$ ) for the three arrays studied here and, therefore, the attenu-  
649 ation structure beneath them. Generally, intrinsic and diffusion quality factors  
650 are lower at all frequencies for ASAR than for the other two arrays, which would  
651 indicate that attenuation caused by these two mechanisms would be strongest for  
652 this array. However, the scattering and total quality factors take similar values for  
653 ASAR and WRA, making their heterogeneity and overall attenuation structure  
654 comparable and different to PSA. These results are consistent with the tectonic  
655 histories and settings of the areas the arrays are located on. WRA and ASAR lie  
656 on the proterozoic North Australian Craton (NAC), but while WRA is situated  
657 near its center, ASAR is on its southern border, a margin with more complex and  
658 recent tectonic history than the interior of the craton, which correlates with the  
659 generally lower quality factor values we observe for ASAR. The EFMD confirms  
660 some of these similarities and differences. Our results suggest the crust is more  
661 heterogeneous than the lithospheric mantle for all arrays, which could be related  
662 to the cratonic nature of the lithosphere in these areas. Correlation lengths in  
663 the crust vary from  $\sim 0.2$ – $1.5$  km and RMS velocity fluctuations take values in the  
664 2–4 % range. The scattering structure of the lithospheric mantle, on the other  
665 hand, is more complex. Solutions for this layer are not unique, with both low  
666 ( $< 2$  km) and high ( $> 5$  km) correlation length values being equally possible. Low

667 velocity fluctuation values are favoured in the inversion results for all arrays, but  
668 the posterior PDFs for ASAR and WRA extend up to  $\sim 6\%$  and  $\sim 7\%$  respectively  
669 and only to  $\sim 3\%$  for PSA, thus supporting our hypothesis that the similarities  
670 and differences in the heterogeneity structure beneath these arrays are caused by  
671 their different locations on the cratons and the different tectonic histories of these  
672 areas.

673 Our study highlights the suitability of Bayesian inversion approaches for the  
674 characterization of lithospheric small-scale structure. The results from our syn-  
675 thetic tests show that the combination of the EFMD and our Bayesian inference  
676 algorithm can effectively recover heterogeneity parameters for 1- and 2-layer mod-  
677 els. Our approach provides detailed information about the parameter space and  
678 the trade offs and uncertainties in the determination of the structural parameters.  
679 The study of the posterior PDFs also allows us to determine whether a single set  
680 of scattering parameters can successfully explain our data or whether solutions are  
681 not unique. This ability makes the Bayesian approach to the EFMD an effective  
682 and useful tool to quantify scattering parameters in the lithosphere.

## 683 **Acknowledgments**

684 This work was supported by the Leeds-York Natural Environment Research Coun-  
685 cil (NERC) Doctoral Training Partnership (DTP) NE/L002574/1, in CASE part-  
686 nership with the Atomic Weapons Establishment (AWE) Blacknest. Andy Nowacki  
687 was supported by NERC (standard grant REMIS: Reliable Earthquake Magnitudes  
688 for Induced Seismicity: NE/R001.154/1).

689 The facilities of IRIS Data Services, and specifically the IRIS Data Manage-  
690 ment Center, were used for access to waveforms, related metadata, and/or derived  
691 products used in this study. IRIS Data Services are funded through the Seismologi-  
692 cal Facilities for the Advancement of Geoscience and EarthScope (SAGE) Proposal  
693 of the National Science Foundation under Cooperative Agreement EAR-1261681.

694 Geoscience Australia operates the Australian National Seismic Network within  
695 Australia, its Territories and across its local region. The network supports the  
696 Joint Australian Tsunami Warning Centre, operated by Geoscience Australia and  
697 the Australian Bureau of Meteorology, which is responsible for issuing tsunami  
698 warning bulletins for Australia and its Territories. The network also contributes  
699 to monitoring earthquakes in the Australian region.

700 Obspy (Krischer et al., 2015) and Matplotlib (Hunter, 2007) were used for data  
701 processing and plotting.

## References

- 702
- 703 Aitken, A. (2009). The architecture, kinematics, and lithospheric processes of  
704 a compressional intraplate orogen occurring under Gondwana assembly: The  
705 Petermann orogeny, central Australia. *Lithosphere*, 1(6):343–357.
- 706 Aitken, A. R. A., Betts, P. G., Weinberg, R. F., and Gray, D. (2009). Constrained  
707 potential field modeling of the crustal architecture of the Musgrave Province in  
708 central Australia: Evidence for lithospheric strengthening due to crust-mantle  
709 boundary uplift. *Journal of Geophysical Research*, 114(B12):B12405.
- 710 Aki, K. (1969). Analysis of the seismic coda of local earthquakes as scattered  
711 waves. *Journal of Geophysical Research*, 74(2):615–631.
- 712 Aki, K. (1973). Scattering of P waves under the Montana Lasa. *Journal of Geo-*  
713 *physical Research*, 78(8):1334–1346.
- 714 Aki, K. and Chouet, B. (1975). Origin of coda waves: Source, attenuation, and  
715 scattering effects. *Journal of Geophysical Research*, 80(23):3322–3342.
- 716 Alexander, S. S. and Phinney, R. A. (1966). A study of the core-mantle boundary  
717 using P waves diffracted by the Earth’s core. *Journal of Geophysical Research*,  
718 71(24):5943–5958.
- 719 Bayes, T. (1763). LII. An essay towards solving a problem in the doctrine of  
720 chances. By the late Rev. Mr. Bayes, F. R. S. communicated by Mr. Price, in a  
721 letter to John Canton, A. M. F. R. S. *Philosophical Transactions of the Royal*  
722 *Society of London*, 53:370–418.
- 723 Blake, D. and Kilgour, B. (1998). Geological Regions of Australia

- 724 1: 5,000,000 Scale [Dataset]. *Geoscience Australia, Canberra. Available at:*  
725 *<http://pid.geoscience.gov.au/dataset/ga/32366>.*
- 726 Brooks, S., German, A., Jones, G., and Meng, X.-L., editors (2011). *Handbook of*  
727 *Markov chain Monte Carlo*. CRC Press.
- 728 Carpenter, E. (1966). A quantitative evaluation of teleseismic explosion records.  
729 *Proceedings of the Royal Society of London. Series A. Mathematical and Physical*  
730 *Sciences*, 290(1422):396–407.
- 731 Cawood, P. and Korsch, R. (2008). Assembling Australia: Proterozoic building of  
732 a continent. *Precambrian Research*, 166(1-4):1–35.
- 733 Chandrasekhar, S. (1950). *Radiative Transfer*. Oxford: Clarendon Press.
- 734 Christensen, N. I. and Mooney, W. D. (1995). Seismic velocity structure and  
735 composition of the continental crust: A global view. *Journal of Geophysical*  
736 *Research: Solid Earth*, 100(B6):9761–9788.
- 737 Clitheroe, G., Gudmundsson, O., and Kennett, B. L. N. (2000). The crustal thick-  
738 ness of Australia. *Journal of Geophysical Research: Solid Earth*, 105(B6):13697–  
739 13713.
- 740 Corbishley, D. J. (1970). Structure under Seismic Arrays. *Geophysical Journal*  
741 *International*, 21(5):415–425.
- 742 Cormier, V. F. (1982). The effect of attenuation on seismic body waves. *Bulletin*  
743 *of the Seismological Society of America*, 72(6B):S169–S200.
- 744 Debayle, E. and Kennett, B. L. N. (2000). The Australian continental upper  
745 mantle: Structure and deformation inferred from surface waves. *Journal of*  
746 *Geophysical Research: Solid Earth*, 105(B11):25423–25450.

- 747 Domínguez, T. and Rebollar, C. J. (1997). Regional variations of seismic attenua-  
748 tion from coda and Lg waves in northern Baja California. *Journal of Geophysical*  
749 *Research: Solid Earth*, 102(B7):15259–15268.
- 750 Drummond, B. and Collins, C. (1986). Seismic evidence for underplating of the  
751 lower continental crust of Australia. *Earth and Planetary Science Letters*, 79(3-  
752 4):361–372.
- 753 Dziewonski, A. M. and Anderson, D. L. (1981). Preliminary reference Earth model.  
754 *Physics of the Earth and Planetary Interiors*, 25(4):297–356.
- 755 Etgen, J., Gray, S. H., and Zhang, Y. (2009). An overview of depth imaging in  
756 exploration geophysics. *Geophysics*, 74(6):WCA5–WCA17.
- 757 Fang, Y. and Müller, G. (1996). Attenuation Operators and Complex Wave Veloci-  
758 ties for Scattering in Random Media. *Pure and Applied Geophysics*, 148(1):269–  
759 285.
- 760 Fehler, M., Hoshihara, M., Sato, H., and Obara, K. (1992). Separation of scat-  
761 tering and intrinsic attenuation for the Kanto-Tokai region, Japan, using mea-  
762 surements of S -wave energy versus hypocentral distance. *Geophysical Journal*  
763 *International*, 108(3):787–800.
- 764 Fichtner, A., Kennett, B. L., Igel, H., and Bunge, H. P. (2009). Full seismic  
765 waveform tomography for upper-mantle structure in the Australasian region  
766 using adjoint methods. *Geophysical Journal International*, 179(3):1703–1725.
- 767 Flatté, S. M. and Wu, R.-S. (1988). Small-scale structure in the lithosphere and as-  
768 thenosphere deduced from arrival time and amplitude fluctuations at NORSAR.  
769 *Journal of Geophysical Research*, 93(B6):6601.

- 770 Ford, H. A., Fischer, K. M., Abt, D. L., Rychert, C. A., and Elkins-Tanton, L. T.  
771 (2010). The lithosphere–asthenosphere boundary and cratonic lithospheric lay-  
772 ering beneath Australia from Sp wave imaging. *Earth and Planetary Science*  
773 *Letters*, 300(3-4):299–310.
- 774 Frankel, A. and Wennerberg, L. (1987). Energy-Flux Model of Seismic Coda:  
775 Separation of Scattering and Intrinsic Attenuation. *Bulletin of the Seismological*  
776 *Society of America*, 77(4):1223–1251.
- 777 Goleby, B. R., Shaw, R. D., Wright, C., Kennett, B. L. N., and Lambeck, K.  
778 (1989). Geophysical evidence for 'thick-skinned' crustal deformation in central  
779 Australia. *Nature*, 337(6205):325–330.
- 780 Hastings, W. K. (1970). Monte Carlo sampling methods using Markov chains and  
781 their applications. *Biometrika*, 57(1):97–109.
- 782 Helmberger, D. V. (1968). The crust-mantle transition in the Bering sea. *Bulletin*  
783 *of the Seismological Society of America*, 58(1):179–214.
- 784 Hock, S. and Korn, M. (2000). Random heterogeneity of the lithosphere across the  
785 Trans-European Suture Zone. *Geophysical Journal International*, 141(1):57–70.
- 786 Hock, S., Korn, M., Ritter, J. R. R., and Rothert, E. (2004). Mapping random  
787 lithospheric heterogeneities in northern and central Europe. *Geophysical Journal*  
788 *International*, 157(1):251–264.
- 789 Hunter, J. D. (2007). Matplotlib: A 2D Graphics Environment. *Computing in*  
790 *Science & Engineering*, 9(3):90–95.
- 791 Kennett, B. (2015). Lithosphere–asthenosphere P-wave reflectivity across Aus-  
792 tralia. *Earth and Planetary Science Letters*, 431:225–235.

- 793 Kennett, B. and Saygin, E. (2015). The nature of the Moho in Australia from  
794 reflection profiling: A review. *GeoResJ*, 5:74–91.
- 795 Kennett, B. and Sippl, C. (2018). Lithospheric discontinuities in Central Australia.  
796 *Tectonophysics*, 744(June):10–22.
- 797 Kennett, B. L., Fichtner, A., Fishwick, S., and Yoshizawa, K. (2013). Australian  
798 seismological reference model (AuSREM): mantle component. *Geophysical Jour-  
799 nal International*, 192(2):871–887.
- 800 Kennett, B. L., Yoshizawa, K., and Furumura, T. (2017). Interactions of multi-  
801 scale heterogeneity in the lithosphere: Australia. *Tectonophysics*, 717:193–213.
- 802 Kennett, B. L. N. and Engdahl, E. R. (1991). Traveltimes for global earthquake lo-  
803 cation and phase identification. *Geophysical Journal International*, 105(2):429–  
804 465.
- 805 Kennett, B. L. N. and Furumura, T. (2016). Multiscale seismic heterogeneity in the  
806 continental lithosphere. *Geochemistry, Geophysics, Geosystems*, 17(3):791–809.
- 807 Kennett, B. L. N. and Salmon, M. (2012). AuSREM: Australian Seismological  
808 Reference Model. *Australian Journal of Earth Sciences*, 59(8):1091–1103.
- 809 Kennett, B. L. N., Salmon, M., Saygin, E., and Group, A. W. (2011). AusMoho:  
810 the variation of Moho depth in Australia. *Geophysical Journal International*,  
811 187(2):946–958.
- 812 Korn, M. (1990). A modified energy flux model for lithospheric scattering of  
813 teleseismic body waves. *Geophysical Journal International*, 102(1):165–175.

- 814 Korn, M. (1993). Determination of Site-Dependent Scattering Q From P -Wave  
815 Coda Analysis With an Energy-Flux Model. *Geophysical Journal International*,  
816 113(1):54–72.
- 817 Korn, M. (1997). Modelling the teleseismic P coda envelope: depth dependent  
818 scattering and deterministic structure. *Physics of the Earth and Planetary In-*  
819 *teriors*, 104(1-3):23–36.
- 820 Korsch, R., Goleby, B., Leven, J., and Drummond, B. (1998). Crustal architecture  
821 of central Australia based on deep seismic reflection profiling. *Tectonophysics*,  
822 288(1-4):57–69.
- 823 Krischer, L., Megies, T., Barsch, R., Beyreuther, M., Lecocq, T., Caudron, C.,  
824 and Wassermann, J. (2015). ObsPy: a bridge for seismology into the scientific  
825 Python ecosystem. *Computational Science & Discovery*, 8(1):014003.
- 826 Langston, C. A. (1989). Scattering of teleseismic body waves under Pasadena,  
827 California. *Journal of Geophysical Research*, 94(B2):1935.
- 828 Mahalanobis, P. C. (1936). On the generalized distance in statistics. National  
829 Institute of Science of India.
- 830 Margerin, L. (2005). Introduction To Radiative Transfer Theory. *Geophysical*  
831 *Monograph-American Geophysical Union*, 157:1–47.
- 832 Metropolis, N., Rosenbluth, A. W., Rosenbluth, M. N., Teller, A. H., and Teller,  
833 E. (1953). Equation of State Calculations by Fast Computing Machines. *The*  
834 *Journal of Chemical Physics*, 21(6):1087–1092.
- 835 Metropolis, N. and Ulam, S. (1949). The Monte Carlo Method. *Journal of the*  
836 *American Statistical Association*, 44(247):335–341.

- 837 Myers, J. S. (1990). Precambrian tectonic evolution of part of Gondwana, south-  
838 western Australia. *Geology*, 18(6):537.
- 839 Randall, G. E. (1994). Efficient calculation of complete differential seismograms  
840 for laterally homogeneous earth models. *Geophysical Journal International*,  
841 118(1):245–254.
- 842 Rautian, T. G. and Khalturin, V. I. (1978). The use of the coda for determination  
843 of the earthquake source spectrum. *Bulletin of the Seismological Society of*  
844 *America*, 68(4):923–948.
- 845 Raymond, O., Totterdell, J., Stewart, A., and Woods, M. (2018). Australian  
846 Geological Provinces, 2018. *Geoscience Australia, Canberra. Available at:*  
847 *<http://pid.geoscience.gov.au/dataset/ga/116823>*.
- 848 Ritter, J. R. R., Shapiro, S. A., and Schechinger, B. (1998). Scattering parameters  
849 of the lithosphere below the Massif Central, France, from teleseismic wavefield  
850 records. *Geophysical Journal International*, 134(1):187–198.
- 851 Salmon, M., Kennett, B., Stern, T., and Aitken, A. (2013a). The Moho in Australia  
852 and New Zealand. *Tectonophysics*, 609:288–298.
- 853 Salmon, M., Kennett, B. L. N., and Saygin, E. (2013b). Australian Seismological  
854 Reference Model (AuSREM): crustal component. *Geophysical Journal Interna-*  
855 *tional*, 192(1):190–206.
- 856 Sato, H. (1977). Energy propagation including scattering effects single isotropic  
857 scattering approximation. *Journal of Physics of the Earth*, 25(1):27–41.
- 858 Sato, H. (1984). Attenuation and envelope formation of three-component seis-

- 859 mograms of small local earthquakes in randomly inhomogeneous lithosphere.  
860 *Journal of Geophysical Research: Solid Earth*, 89(B2):1221–1241.
- 861 Sato, H., Fehler, M. C., and Maeda, T. (2012). *Seismic Wave Propagation and*  
862 *Scattering in the Heterogeneous Earth : Second Edition*. Springer Berlin Hei-  
863 delberg, Berlin, Heidelberg.
- 864 Shapiro, S. A. and Kneib, G. (1993). Seismic Attenuation By Scattering: Theory  
865 and Numerical Results. *Geophysical Journal International*, 114(2):373–391.
- 866 Shearer, P. M. and Earle, P. S. (2004). The global short-period wavefield modelled  
867 with a Monte Carlo seismic phonon method. *Geophysical Journal International*,  
868 158(3):1103–1117.
- 869 Simons, F. J., Zielhuis, A., and der Hilst, R. D. (1999). The deep structure of the  
870 Australian continent inferred from surface wave tomography. *Lithos*, 48:17–43.
- 871 Sipkin, S. A. and Revenaugh, J. (1994). Regional variation of attenuation and  
872 travel time in china from analysis of multiple-scs phases. *Journal of Geophysical*  
873 *Research: Solid Earth*, 99(B2):2687–2699.
- 874 Sippl, C. (2016). Moho geometry along a north-south passive seismic transect  
875 through Central Australia. *Tectonophysics*, 676:56–69.
- 876 Tarantola, A. (2005). *Inverse problem theory and methods for model parameter*  
877 *estimation*, volume 89. Siam.
- 878 Thorbecke, J., Slob, E., Brackenhoff, J., van der Neut, J., and Wapenaar, K.  
879 (2017). Implementation of the Marchenko method. *Geophysics*, 82(6):WB29–  
880 WB45.

- 881 van der Neut, J., Wapenaar, K., Thorbecke, J., Slob, E., and Vasconcelos, I.  
882 (2015). An illustration of adaptive Marchenko imaging. *The Leading Edge*,  
883 34(7):818–822.
- 884 Wellman, P. (1998). Mapping of geophysical domains in the Australian continental  
885 crust using gravity and magnetic anomalies. In *Structure and evolution of the*  
886 *Australian continent*, pages 59–71. American Geophysical Union, Washington,  
887 D.C: AGU.
- 888 Wu, R.-S. (1985). Multiple scattering and energy transfer of seismic waves – sepa-  
889 ration of scattering effect from intrinsic attenuation – I. Theoretical modelling.  
890 *Geophysical Journal International*, 82(1):57–80.
- 891 Wu, R.-S. and Aki, K. (1988). Introduction: Seismic Wave Scattering in Three-  
892 dimensionally Heterogeneous Earth. In *Scattering and Attenuations of Seismic*  
893 *Waves, Part I*, pages 1–6. Birkhäuser Basel, Basel.
- 894 Yoshizawa, K. and Kennett, B. L. N. (2015). The lithosphere-asthenosphere tran-  
895 sition and radial anisotropy beneath the Australian continent. *Geophysical Re-*  
896 *search Letters*.
- 897 Zelt, C. A. and Barton, P. J. (1998). Three-dimensional seismic refraction tomog-  
898 raphy: A comparison of two methods applied to data from the Faeroe Basin.  
899 *Journal of Geophysical Research: Solid Earth*, 103(B4):7187–7210.

## 900 S SUPPLEMENTARY MATERIAL

### 901 S.1 Additional synthetic tests results

902 Figures S1 and S2 contain the results from our synthetic tests for models 3 and  
 903 4 on Table 2. Both of them are two-layer models, so three independent Markov  
 904 chains, each one 3 million iterations long, were combined to produce these figures.

905 Figure S3 contains the marginal PDFs for all parameters in all layers, as well  
 906 as the PDF for each individual parameter. These plots illustrate the presence of  
 907 two independent families of parameters that separately fit our data within our  
 908 posterior PDFs. Subindices  $Li$  ( $i$  being the layer number) are used here to refer  
 909 to parameter values in each layer of the model. Starting on panel 3–1, we observe  
 910 how all accepted models corresponding to  $a_{L1} \sim 1$  km (the sharp peak on panel  
 911 1–1) have  $a_{L2}$  values either lower than 1 km or higher than 2 km, which would  
 912 correspond to the tails of the  $a_{L2}$  PDF on panel 3–3. Panel 3–2 compares  $\epsilon_{L1}$  and  
 913  $a_{L2}$  and we can see how all models with  $a_{L2}$  in the ranges mentioned before have  
 914  $\epsilon_{L1} > 3.5\%$ . Similarly, panels 4–1, 5–2 and 5–3 show that these values of  $a_{L1}$ ,  $a_{L2}$   
 915 and  $\epsilon_{L1}$  correspond to  $\epsilon_{L2} < \sim 5\%$ ,  $\epsilon_{L3} \sim 2.1\%$  (the second, sharp, peak on the  
 916 PDF on panel 6–6) and  $2 < a_{L3} < 10$  km (the wide peak on the PDF on panel  
 917 5–5). Interestingly, the first peak and the side tail on the  $\epsilon_{L3}$  PDF (panel 6–6)  
 918 correspond to the same parameter family, as do the tail and the base of the peak  
 919 on the  $a_{L3}$  PDF (panel 5–5). Following the same reasoning detailed above, we  
 920 extracted the other family of parameters, which are summarised on Table S1.

921

**Table S1:** Summary of the two independent and equally likely families of parameters extracted from Fig. S3 for our synthetic model 3 from Table 2.

	$a_{L1}$ (km)	$\epsilon_{L1}$ (%)	$a_{L2}$ (km)	$\epsilon_{L2}$ (%)	$a_{L3}$ (km)	$\epsilon_{L3}$ (%)
Input model	1.0	4.0	2.0	3.0	4.0	2.0
Parameter family 1	$\sim 1$	$> 3.5\%$	$< 1 \ \& \ > 2$	$< 5$	2–10	$\sim 2.1$
Parameter family 2	$< 0.6 \ \& \ > 1.1$	$< 3.5$	$\sim 1.2$	$\sim 6$	3–30	$\sim 1.6\text{--}3.7$

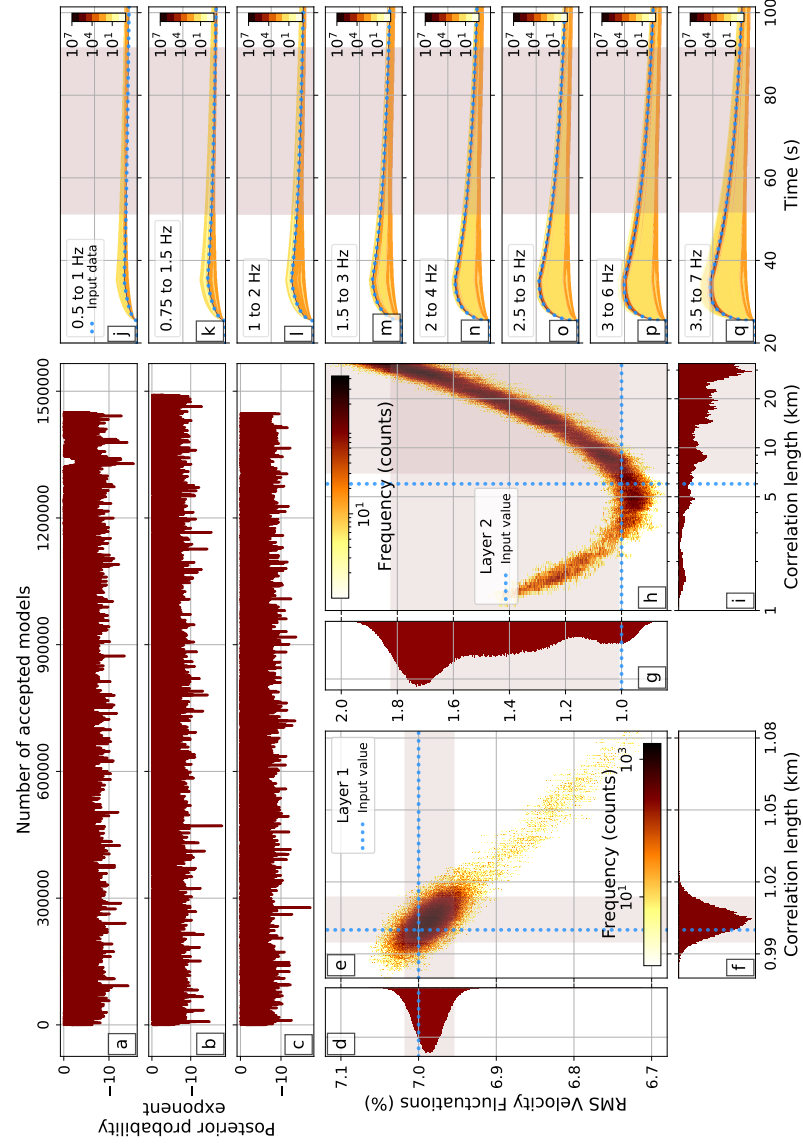


Figure S1: Results from our synthetic test of model 3 from Table 2, in which a strongly scattering layer lies above a weakly scattering one. Panels a–c show the loglikelihood for each accepted model in the chain, while d–i contain the posterior PDFs of the structural parameters and the joint PDF. Dotted blue lines in these plots represent the input parameter values and the shaded area indicates the 5–95 percentile range (PR). Panels j–q on the right contain 2D histograms of the synthetic envelopes for all accepted models, with color bars indicating the number of models that produced a data sample within each bin of the grid. Vertical scale is the same in all plots. The shaded area in these panels points to the extent of the time window used for the fitting.

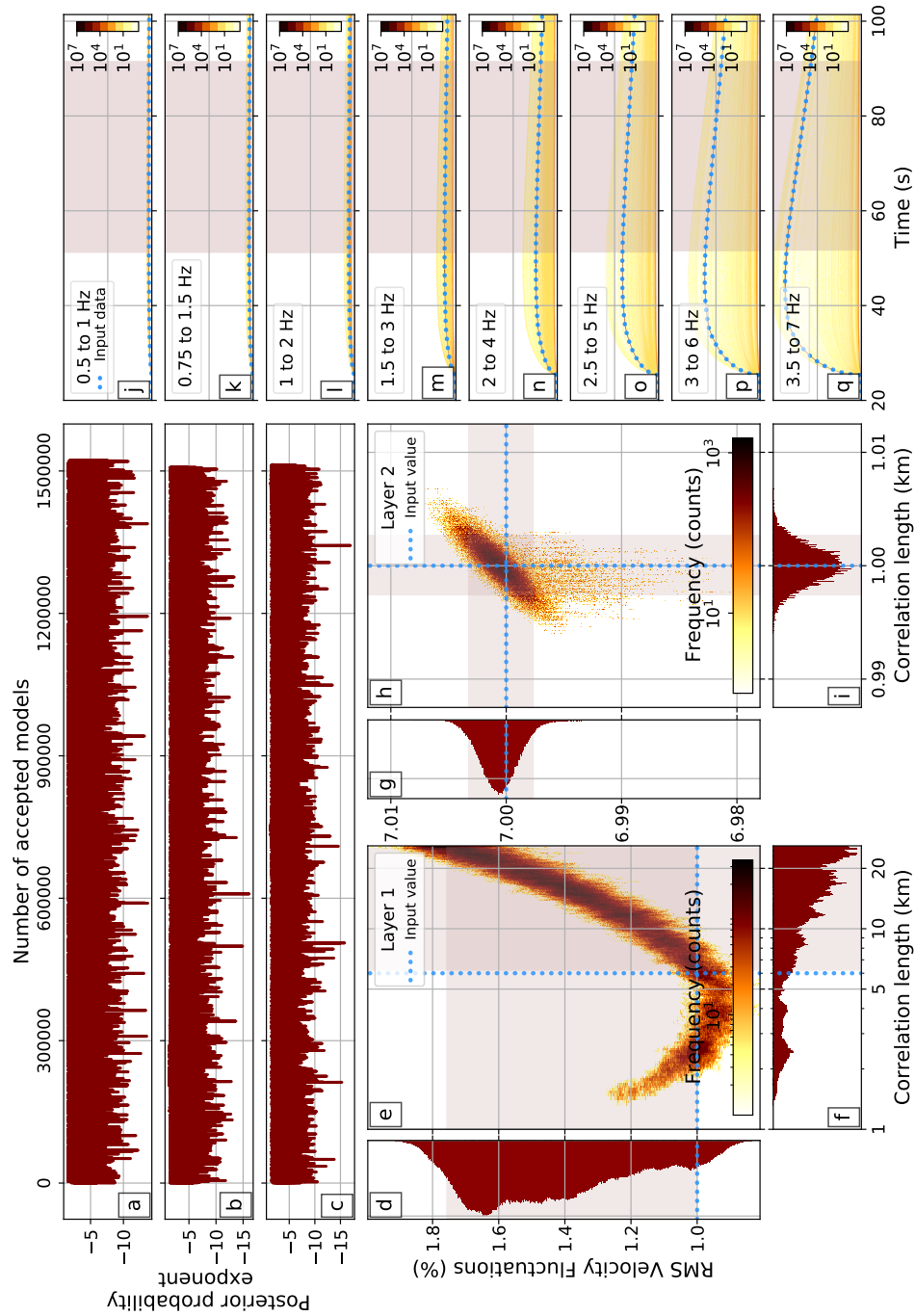


Figure S2: Results from our synthetic test of model 4. In this case, the top layer contains weak heterogeneities, while the bottom layer is highly heterogeneous.

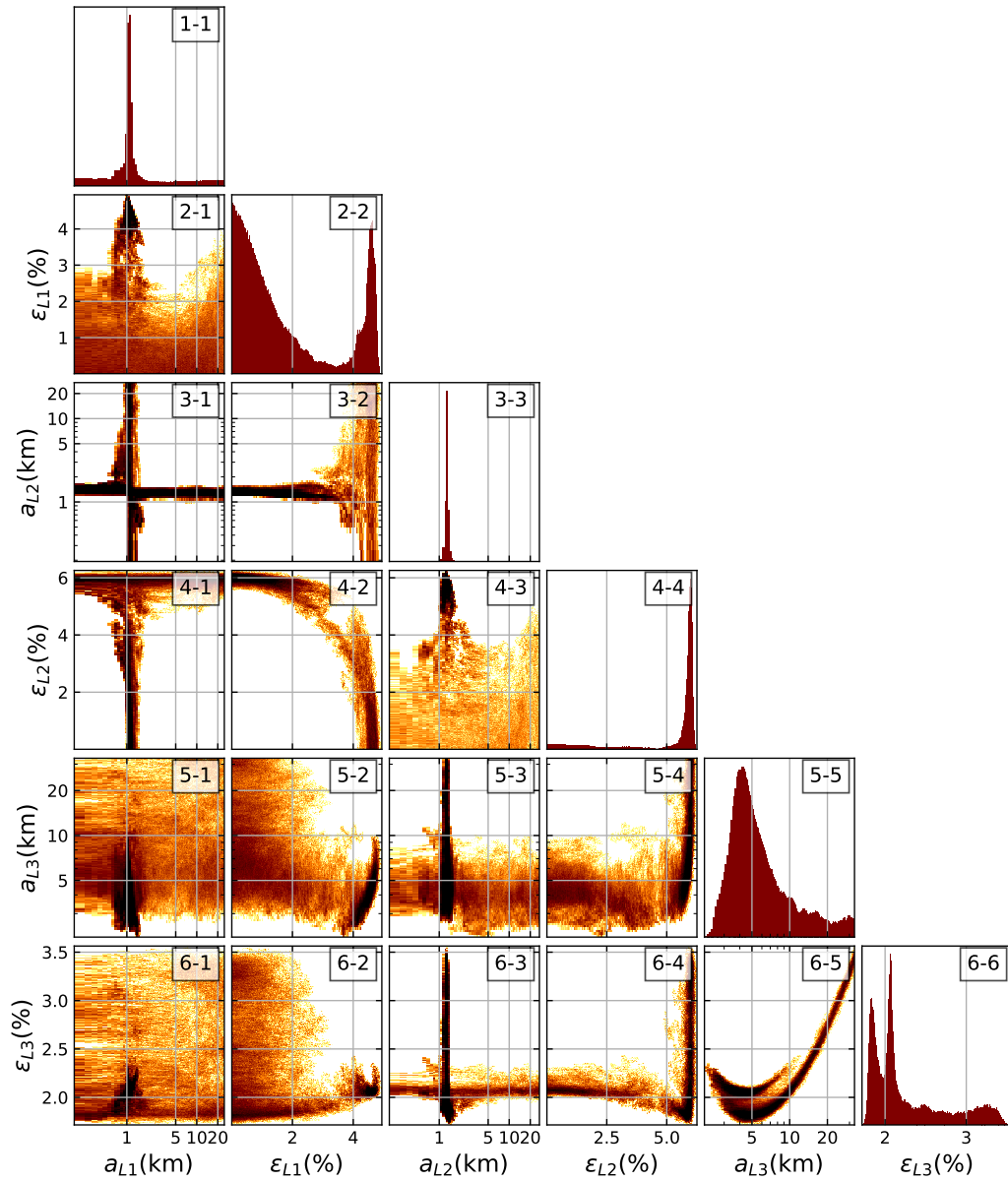


Figure S3: Joint PDFs for all parameters and layers in synthetic model 5 from Table 2. Plots in the diagonal of the figure contain the individual PDF for the different scattering parameters.

## 922 S.2 Additional EFM results

923 Figures S4, S5 and S6 show our results from the different least-squares fits neces-  
 924 sary to obtain our final EFM results, as described in Section 2.1.

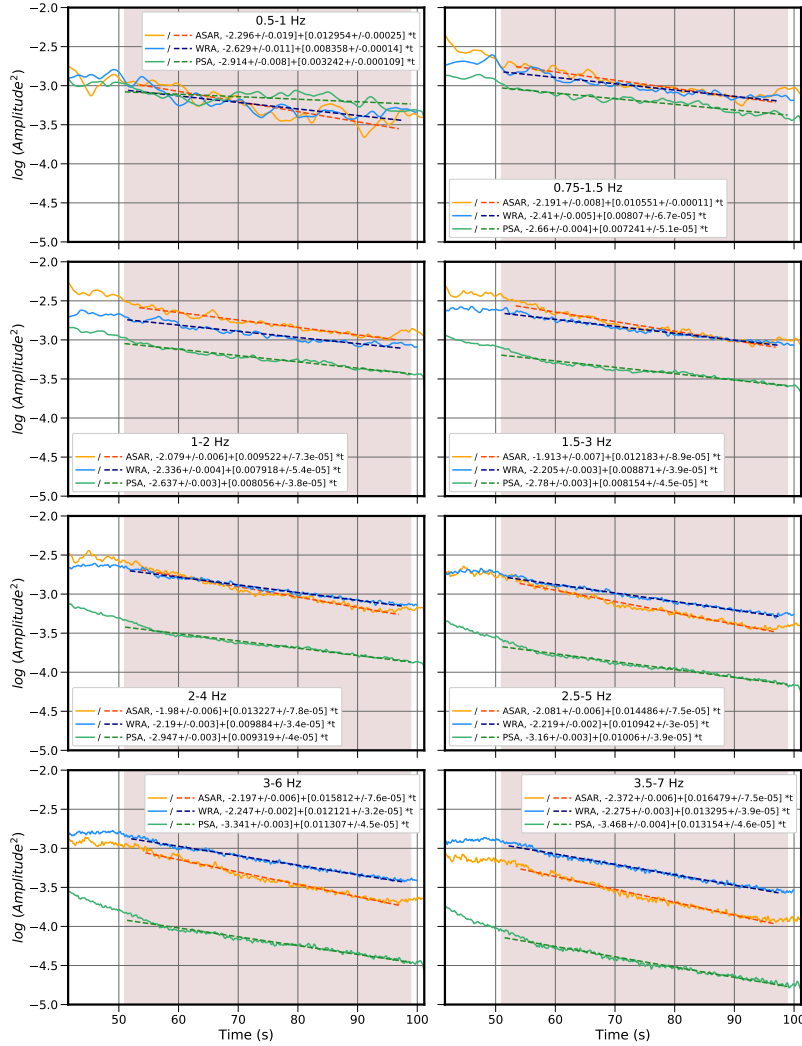


Figure S4: Linear fit of the logarithm of the squared normalised coda envelopes for all arrays, as described in Section 2.1. The shaded area represents the maximum time window used for the fits. Lighter solid lines represent our data envelopes. Darker, dashed lines show the linear fits whose equations are shown in the legend.

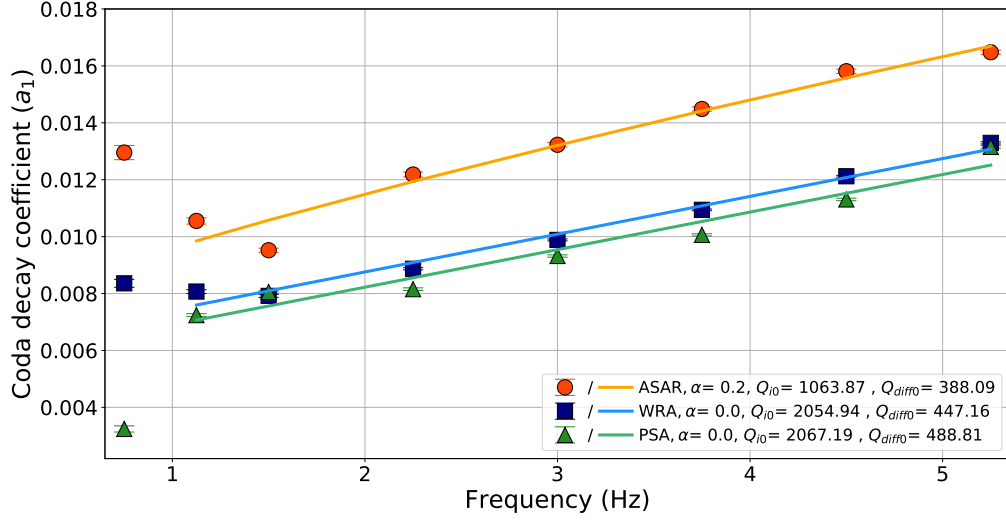


Figure S5: Coda decay coefficient ( $a_1$ ) vs. frequency for all arrays. Solid lines represent the regression curves defined by Eq. 18 from Korn (1990). The legend contains our obtained values of the intrinsic and diffusion quality factors at 1 Hz, as well as the indicative estimation of the thickness of the scattering layer.

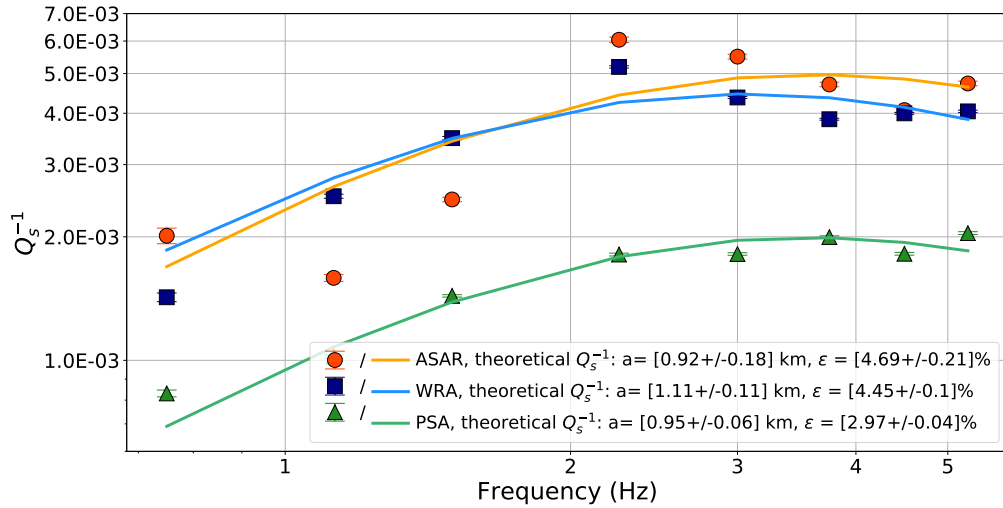


Figure S6: Scattering quality factor,  $Q_s$ , vs. the theoretical curve derived by Fang and Müller (1996). The legend contains our estimation of the correlation length and RMS velocity fluctuations for a single scattering layer.

### 925 **S.3 Additional EFMD results**

926 Results from EFMD inversions from our initial tests. In all cases, three indepen-  
 927 dent Markov chains have been combined to produce these results, each one 1 or  
 928 3 million iterations long for models with 1 or 2 layers respectively. The burn in  
 929 phase has been removed from all of them, as described in Section 2.2.2. Panel  
 930 content in all these figures is as described in Section S.1.

931 We used the relationship between  $Q_s^{-1}$  and the structural parameters derived  
 932 by Fang and Müller (1996) to calculate the scattering quality factor for each array,  
 933 frequency band and model layer. The 5 – 95 percentile range (PR) for each pa-  
 934 rameter provides minimum and maximum  $Q_s$  values for each layer. The equation  
 935 below, based on the definition of attenuated time given by Carpenter (1966), al-  
 936 lows us to calculate the average scattering quality factor for the lithosphere, which  
 937 we can then compare with our  $Q_s$  values from the EFM:

$$\frac{t_{total}}{Q_{saverage}} = \frac{t_1}{Q_{s1}} + \frac{t_2}{Q_{s2}}, \quad (\text{S1})$$

938 where  $t_{total}$  represents the total travelttime through the lithosphere and  $t_i$  and  $Q_{s_i}$   
 939 ( $i = 1, 2$ ) the travelttime and scattering quality factor for each layer in the model  
 940 respectively. Figure S10 shows a comparison between our EFM  $Q_s$  values for the  
 941 single-layer model and the ones calculated for the EFMD using Eq. S1.

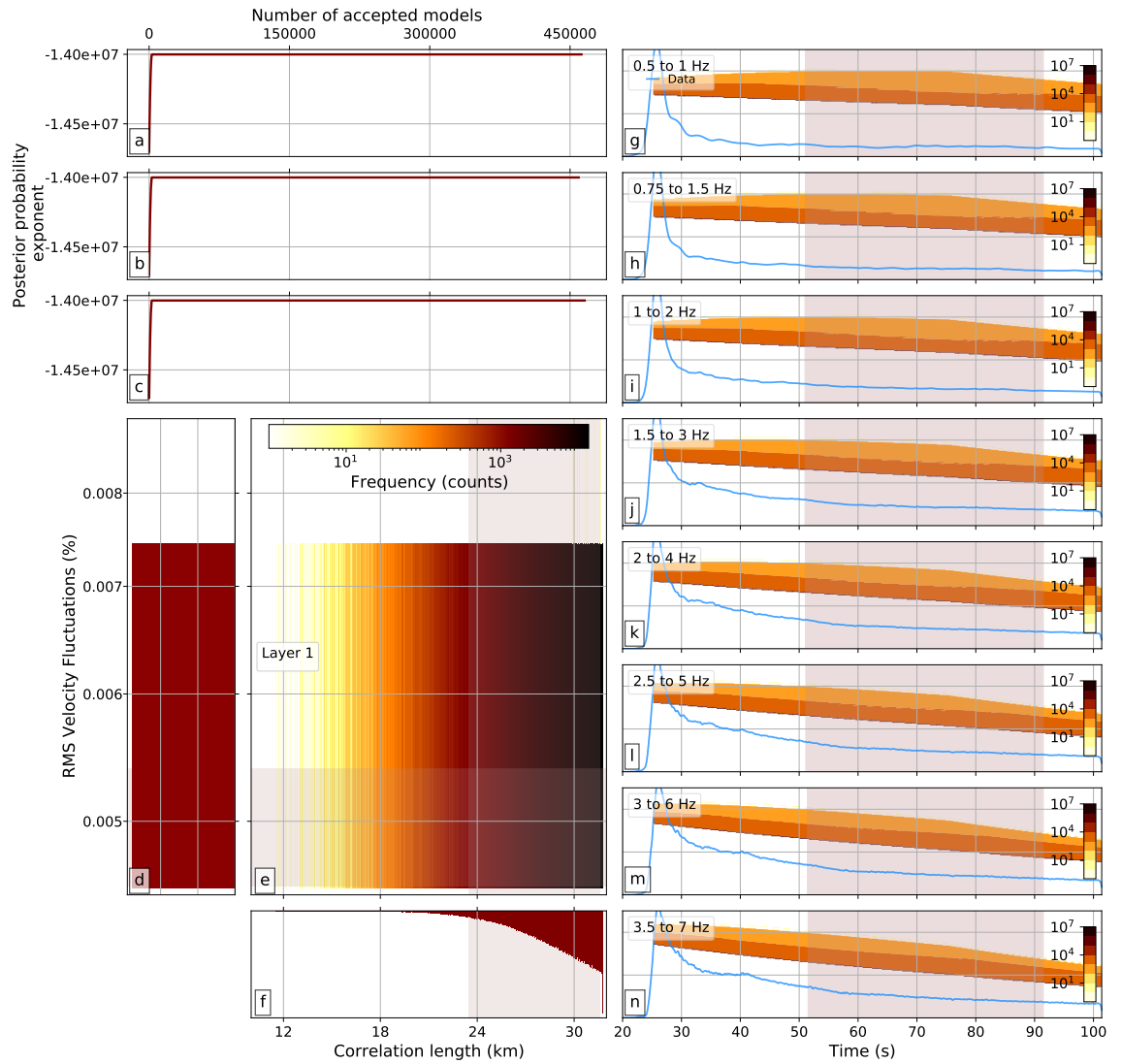


Figure S7: EFMD results for PSA and model type I.

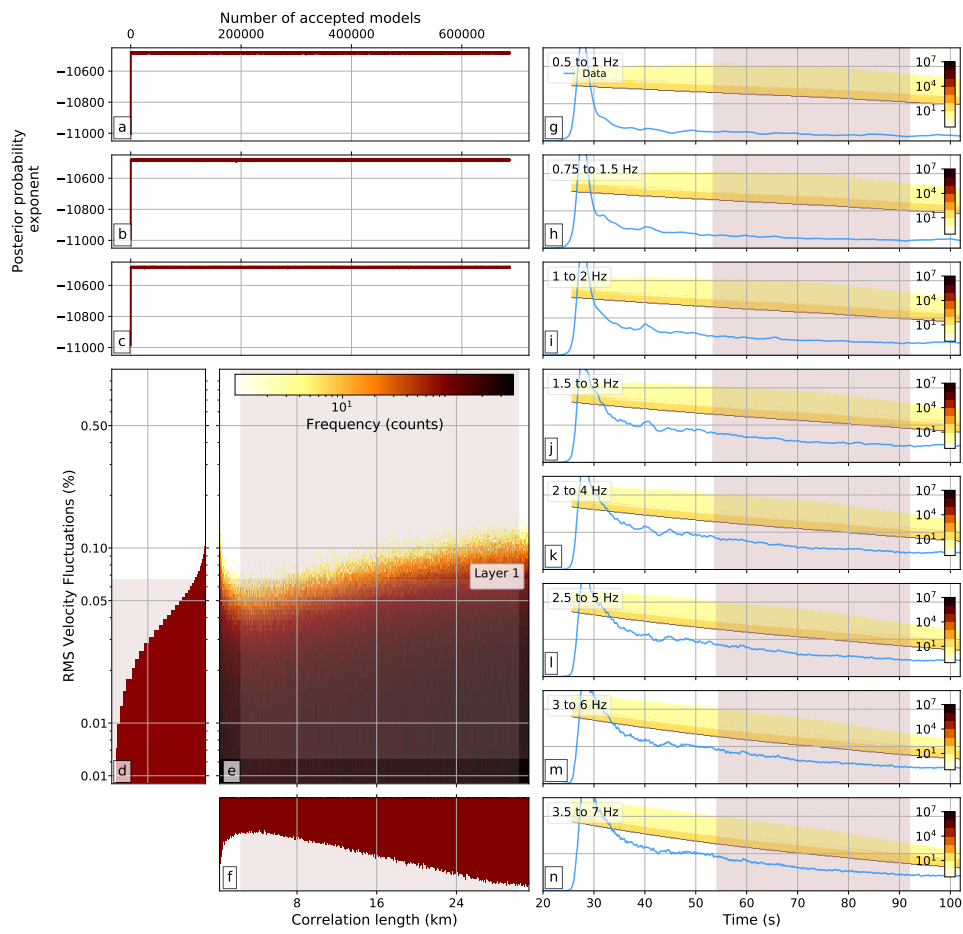


Figure S8: EFMD results for ASAR and model type I.

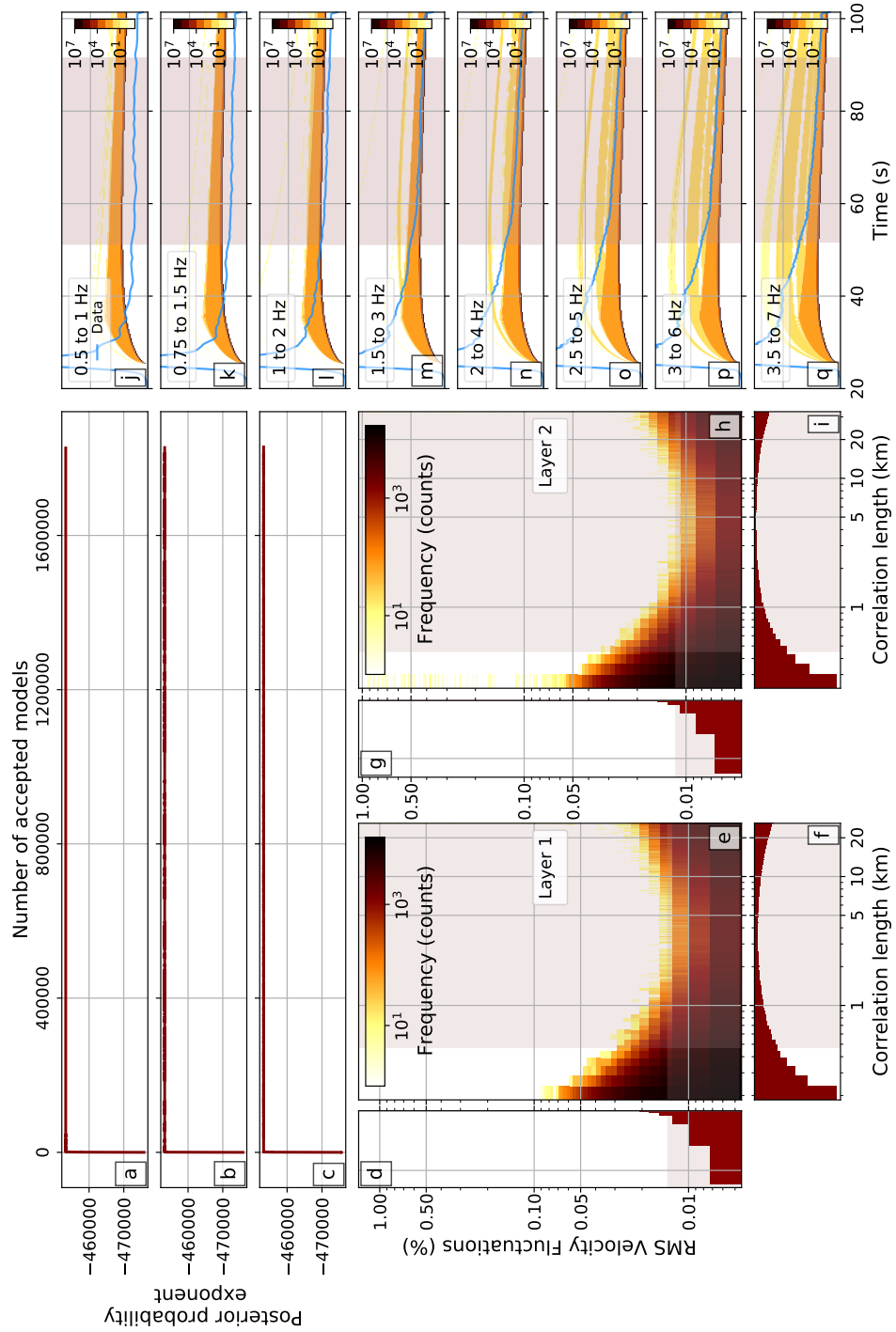


Figure S9: EFMD results for PSA and model type II using all eight frequency bands listed on Table 1.

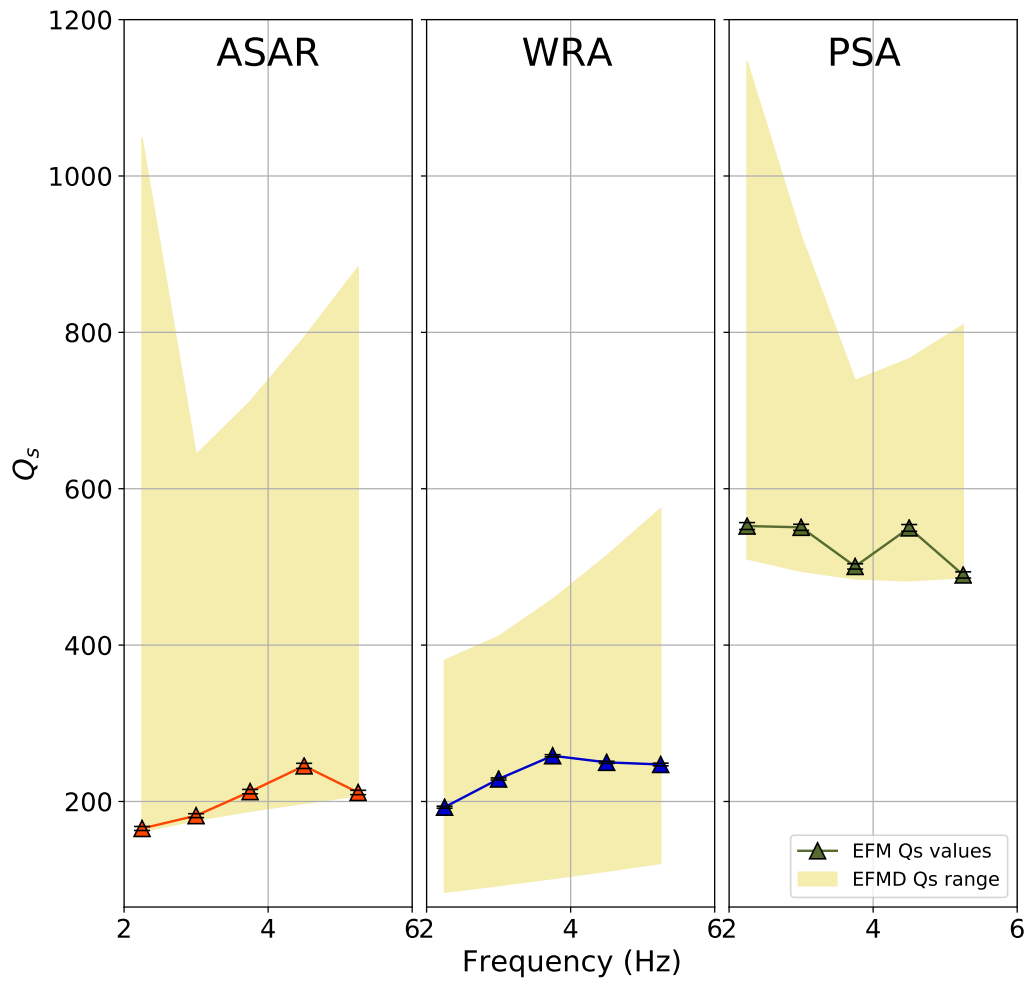


Figure S10: Comparison between the  $Q_s$  values obtained from the EFM and calculated from the EFMD structural parameters. Shaded area represents the range between the minimum and maximum  $Q_s$  values, derived using the lower and higher ends of the 5 – 95 PR for each parameter in each layer and Eq. S1.